Investigation of Variable Switching Frequency in Finite Control Set Model Predictive Control on Grid-Connected Inverters

Luocheng Wang, *Student Member, IEEE*, Tiefu Zhao, *Senior Member, IEEE*, and Jiangbiao He, *Senior Member, IEEE*

Abstract: Finite control set model predictive control (FCS-MPC) has been widely studied and applied to the power converters and motor drives. It provides the power electronics system with fast dynamic response, nonlinear system formulation, and flexible objectives and constraints integration. However, its variable switching frequency feature also induces severe concerns on the power loss, the thermal profile, and the filter design. Stemming from these concerns, this article investigates the variable switching frequency characteristics of FCS-MPC on the grid-connected inverters. An intuitive relationship between the switching frequency and the magnitude of the converter output voltage is proposed through the geometry analysis, where the switching frequency is maximized when the converter output voltage is around one-third of the DC bus voltage and decreasing when the output voltage moves away from this value. The impacts of this variable switching frequency property on the power loss and current harmonics are also analyzed. Simulation and experimental results both verify the proposed property. With this intrinsic property, FCS-MPC can autonomously achieve a less-varying temperature profile of power modules and an improved reliability compared with the conventional control strategy.

***Index Terms*—Finite control set model predictive control, geometry analysis, grid-connected inverter, power loss, switching frequency, switching state, voltage vector space.**

I. Introduction

Power converters are playing a significant role in the distributed energy resource (DER) systems to transmit and synchronize the power from the front-end renewable energy mechanisms to the main utility grid. The most common layout in these DER systems is designed with a grid side converter unit which is interconnected between the DC bus and the main utility grid [1]. The grid side converter is oriented to synchronize the real power from the active front end, such as the wind turbine in the wind power or the PV panel in the solar energy, stably to the main utility grid.

In order to improve the performance of these DER systems, the research on the advanced converter control strategies has never stopped. In addition to the conventional linear proportional-integral (PI) or proportional-resonant (PR) control [1], [2], fuzzy control [3], adaptive control [4], sliding mode control [5] and other intelligent controls [6] are all being investigated. Among all, benefiting from the rapid development of the microprocessor units, the model predictive control (MPC) is growing most significantly in the past decade [7]-[14]. It has been gradually categorized into the indirect MPC and direct MPC [14] depending on whether it needs a conventional modulation to determine the switching state. Further, calibrated with the intuitive design and straightforward implementation, the finite control set MPC (FCS-MPC) as the direct MPC becomes one of the most favored control strategies in current researches [10], [15]-[20]. With significant features of the fast dynamic response, the nonlinear system formulation, and the multiple objectives and constraints integration, FCS-MPC has been widely adopted in power electronics systems for applications in, but not limited to, power flow control, motor drives, AC voltage or uninterruptible power supply control, grid service, and loss and thermal control [21]-[33].

However, one controversial property of FCS-MPC is its variable switching frequency. FCS-MPC explicitly selects the optimal switching state based on the present and the predicted future system behaviors, where the modulation scheme is not required. Without the modulation scheme, the switching states are not forced to transit at a specific frequency, and only transit when FCS-MPC selects different switching states. Hence, the switching transitions become indefinite and the switching frequency varies with the steady state of the power converter. One advantage of this variable switching frequency property is to provide the power converter with a new degree of freedom, that the switching frequency can be easily adjusted. An additional objective function is integrated in [28] and [29] for the power loss, where FCS-MPC heuristically levels the power loss by decreasing the switching frequency in high power loadings and relieve the thermal stress on power semiconductor devices. A similar idea is also adopted in [30], where FCS-MPC selects the optimal switching state only from a set of the fewer switching events for a lower switching loss.

Most of other time, this unclear variable switching frequency property of FCS-MPC adversely affects the power electronics systems. Since the switching frequency is varying

This article has been accepted for publication in a future issue of this journal, but has not been fully edited. Content may change prior to final publication. Citation information: DOI 10.1109/OJIA.2021.3091154, IEEE Open Journal of Industry Applications

with the steady state of the power converter, the switching loss could not be analytically specified in the design stage. In other words, it prevents the designers from estimating the accurate total power loss, which brings huge difficulties in the thermal management and power derating. Another disadvantage happens to the line filter design. The high-order harmonics will be much more dynamic on the spectrum, whereas the cutoff frequency and bandwidth are static for a fixed line filter. Thereby, a stricter filter design has to be considered to cover a wider frequency spectrum for the converter controlled by FCS-MPC.

Suffering from these impacts of the variable switching frequency property, several researchers manipulate the problem formulation or add a switching penalty objective function to either fix or limit the switching frequency [34]-[41]. By such means, the variable switching frequency property of FCS-MPC has been avoided. However, there are still some applications not involving the switching penalty objective function in the problem formulation [22]-[25], [42]-[44]. This may result from the multilevel converter topology [42], where the switching frequency may not be consistent for all active switches. In cases of the high order system modeling [22]-[24], [43], and the critical current vector control [25], [44], the switching penalty objective function may downgrade the vector control. The current vector control is the only objective function in those problem formulations and the variable switching frequency exists. To better deal with these situations, the variable switching frequency property of FCS-MPC requires a full investigation and its impact on the power converter operation needs to be identified sufficiently.

In this paper, the variable switching frequency property of FCS-MPC is investigated. In FCS-MPC, it is the problem formulation, which consists of the objective functions, the input variables and the constraints, that determines the steady state of the power converter, including the specific switching frequency. At this point, the basic problem formulation with the current vector objective function, which is widely used in power electronics systems, is focused in this paper. First, an intuitive relationship between the switching frequency and the magnitude of the converter output voltage is proposed to qualitatively reveal the change of the switching frequency. Then, steady states of the power converter are translated into operating points on the voltage vector space and are contoured for validation. Moreover, the impacts of this property on the power loss and the current harmonics are also analyzed, which enrich the state of the art with more insights to fully leverage the FCS-MPC.

The rest content of this paper is organized as follows: the variable switching frequency property of FCS-MPC is investigated in Section II. Section III contours the feasible operation range of the grid-connected inverter on the voltage vector space. The simulation results are presented in Section IV based on a 1-MVA DER system. The experimental validations and one application to reduce the thermal stress are given in Section V, and conclusions come to the last.

II. Variable Switching Frequency of FCS-MPC

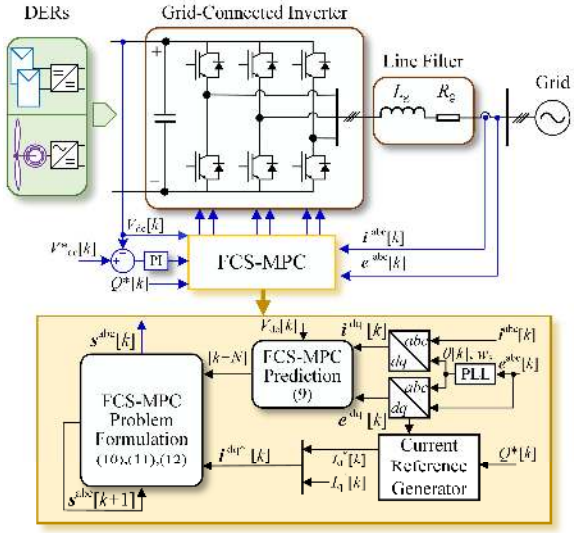

Fig. 1 System diagram of the GCI regulated by FCS-MPC with the basic problem formulation.

With the finite number of switching states from the power converter, FCS-MPC heuristically selects the optimal switching state among all candidates. The selection of the optimal state is determined by minimizing the objective function from the defined problem formulation. In this paper, this basic problem formulation which only contains the current objective function is deeply investigated to reveal the variable switching frequency property of FCS-MPC.

The control block diagram of FCS-MPC with the basic problem formulation is presented in Fig. 1. A two-level three-phase voltage source converter is interconnected between an AC grid and a DC bus as the grid-connected inverter (GCI), where its line current $\boldsymbol{i}^{\mathrm{abc}} \in \mathbb{R}^{3\mathrm{x}1}$ is regulated to synchronize with the grid voltage $\boldsymbol{e}^{\mathrm{abc}} \in \mathbb{R}^{3\mathrm{x}1}$ and transmit all the real power to the grid. The regulation of the DC bus voltage V_{dc} is added on the periphery of this block diagram, but is not included in the analysis since it does not affect the problem formulation in the FCS-MPC, only interfere in the current reference $\boldsymbol{i}^{\mathrm{dq}*} \in \mathbb{R}^{2\mathrm{x}1}$ in the transient state. The L type line filter is used in this paper since it's still being used in the industry [48], [49], and the different types of line filter would not affect the proposed variable switching frequency property, but the operating point of GCI. The system modeling with the *LCL* type line filter will be investigated in the future work. FCS-MPC selects the optimal switching state and directly outputs to the gate drive circuit with no modulation process, which generates the indefinite switching transitions and the variable switching frequency.

A. System modeling of Grid-Connected Inverter

In order to investigate the variable switching frequency of FCS-MPC, the selection of the optimal switching state is fully comprehended through the algorithm of FCS-MPC and the geometry analysis. Then the switching sequence and transition will be discussed in the following section. Before that, the system modeling is introduced first in the rotating *dq* reference frame to explain the algorithm of FCS-MPC,

This article has been accepted for publication in a future issue of this journal, but has not been fully edited. Content may change prior to final publication. Citation information: DOI 10.1109/OJIA.2021.3091154, IEEE Open Journal of Industry Applications

$$L_{\mathrm{g}}\begin{bmatrix}\dfrac{dI_{\mathrm{d}}}{dt}\\ \dfrac{dI_{\mathrm{q}}}{dt}\end{bmatrix}=\begin{bmatrix}V_{\mathrm{d}}\\ V_{\mathrm{q}}\end{bmatrix}-\begin{bmatrix}E_{\mathrm{d}}\\ E_{\mathrm{q}}\end{bmatrix}-R_{\mathrm{g}}\begin{bmatrix}I_{\mathrm{d}}\\ I_{\mathrm{q}}\end{bmatrix}-w_{\mathrm{s}}L_{\mathrm{g}}\begin{bmatrix}-I_{\mathrm{q}}\\ I_{\mathrm{d}}\end{bmatrix} \quad (1)$$

$$\mathbf{T}\triangleq\begin{cases}\boldsymbol{x}^{\mathrm{dq}}=\begin{bmatrix}X_{\mathrm{d}}\\ X_{\mathrm{q}}\end{bmatrix}=\begin{bmatrix}\sin(w_s t) & -\cos(w_s t)\\ \cos(w_s t) & \sin(w_s t)\end{bmatrix}\cdot\boldsymbol{x}^{\alpha\beta}\\ \boldsymbol{x}^{\alpha\beta}=\dfrac{2}{3}\begin{bmatrix}1 & -1/2 & -1/2\\ 0 & \sqrt{3}/2 & -\sqrt{3}/2\end{bmatrix}\cdot\boldsymbol{x}^{\mathrm{abc}}\end{cases} \quad (2)$$

where R_{g} and L_{g} are line resistance and inductance, respectively, w_{s} is the synchronous angular speed of the AC grid. $\boldsymbol{e}^{\mathrm{abc}}$, $\boldsymbol{i}^{\mathrm{abc}}$, and the GCI output voltage $\boldsymbol{v}^{\mathrm{abc}}\in\mathbb{R}^{3\mathrm{x}1}$ are transformed into the synchronous *dq* reference variables $\boldsymbol{e}^{\mathrm{dq}}\in\mathbb{R}^{2\mathrm{x}1}$, $\boldsymbol{i}^{\mathrm{dq}}\in\mathbb{R}^{2\mathrm{x}1}$, $\boldsymbol{v}^{\mathrm{dq}}\in\mathbb{R}^{2\mathrm{x}1}$, respectively, by (2). The GCI output voltage $\boldsymbol{v}^{\mathrm{abc}}$ is given in the voltage vector space as

$$\boldsymbol{v}^{\mathrm{abc}}=V_{\mathrm{dc}}\cdot\frac{1}{3}\begin{bmatrix}2 & -1 & -1\\ -1 & 2 & -1\\ -1 & -1 & 2\end{bmatrix}\boldsymbol{s}^{\mathrm{abc}} \quad (3)$$

where

$$\boldsymbol{s}^{\mathrm{abc}}\in S:=\{(000),(100),(110),(010),(011),(001),(101),(111)\} \quad (4)$$

$\boldsymbol{s}^{\mathrm{abc}}$ represents eight switching states of the two-level GCI. Equations (1)-(3) can be rewritten as a state-space system

$$\frac{d\boldsymbol{i}^{\mathrm{dq}}}{dt}=A\boldsymbol{i}^{\mathrm{dq}}+B\boldsymbol{u}^{\mathrm{dq}} \quad (5)$$

where

$$\boldsymbol{i}^{\mathrm{dq}}=[I_{\mathrm{d}}\ \ I_{\mathrm{q}}]^T,\ \boldsymbol{u}^{\mathrm{dq}}=[V_{\mathrm{d}}\ V_{\mathrm{q}}\ E_{\mathrm{d}}\ E_{\mathrm{q}}]^T \quad (6)$$

$$A=\begin{bmatrix}-\dfrac{R_{\mathrm{g}}}{L_{\mathrm{g}}} & w_{\mathrm{s}}\\ -w_{\mathrm{s}} & -\dfrac{R_{\mathrm{g}}}{L_{\mathrm{g}}}\end{bmatrix} \quad (7)$$

$$B=\begin{bmatrix}\dfrac{1}{L_{\mathrm{g}}} & 0 & -\dfrac{1}{L_{\mathrm{g}}} & 0\\ 0 & \dfrac{1}{L_{\mathrm{g}}} & 0 & -\dfrac{1}{L_{\mathrm{g}}}\end{bmatrix} \quad (8)$$

The state variables in (5) are predicted by discrete Euler's forward formula in the receding horizon, which is described by the following equation:

$$\boldsymbol{i}^{\mathrm{dq}}[k+H]=\boldsymbol{i}^{\mathrm{dq}}[k]+T_{\mathrm{s}}\sum_{j=0}^{H-1}\frac{d\boldsymbol{i}^{\mathrm{dq}}[k+j]}{dt} \quad (9)$$

where k is the discrete time instant, H is the prediction receding horizon and T_{s} is the sampling period. H is set to be one, because the fundamental frequency of the grid voltage is much smaller than the sampling frequency and the first order filter is used. One discrete time instant is sufficient to predict the state variables and consumes the least online calculation from microprocessors.

The predicted values from (9) are transmitted to the problem formulation of FCS-MPC. Since the fundamental target of GCIs is to regulate the line current for the power flow control, the basic problem formulation is described as:

$$\min_{s^{abc}}\ J=\sum_{j=1}^{H}\|\boldsymbol{i}^{\mathrm{dq}*}[k]-\boldsymbol{i}^{\mathrm{dq}}[k+j]\|_2^2 \quad (10)$$

s.t.

$$\mathcal{C}_1\colon\ \|\boldsymbol{v}^{\mathrm{dq}}[k+j]\|_2\le V_{\mathrm{dc}}/\sqrt{3}\quad\text{for}\quad j=1,\ldots,H \quad (11)$$

$$\mathcal{C}_2\colon\ \|\boldsymbol{i}^{\mathrm{dq}}[k+j]\|_2\le I_{\max}\quad\text{for}\quad j=1,\ldots,H \quad (12)$$

where J and C denote the objective function and the constraint function, respectively, the input variable is $\boldsymbol{s}^{\mathrm{abc}}$ defined in (4) and $I_{\max}$ is the maximum continuous current from either the datasheet of the power module or designed power loading. In this paper, a norm-2 ℓ_2 least square objective function is used in (10) due to its differentiability for the later mathematical derivation. By specifying H = 1, (10) is expressed as

$$J=\|\boldsymbol{i}^{\mathrm{dq}*}[k]-\boldsymbol{i}^{\mathrm{dq}}[k+1]\|_2^2 \quad (13)$$

Eventually, the basic problem formulation is fulfilled by combining (10)-(13).

B. Switching State Selection of FCS-MPC

FCS-MPC selects the optimal switching state by minimizing the objective function (13). In order to clarify this selection, (13) is expanded as,

$$J=(I_{\mathrm{d}}^*[k]-I_{\mathrm{d}}[k+1])^2+(I_{\mathrm{q}}^*[k]-I_{\mathrm{q}}[k+1])^2 \quad (14)$$

Then, the predicated state variables in (14) are replaced by (9), and (14) turns into

$$\begin{aligned}J=&\left(I_{\mathrm{d}}^*[k]-I_{\mathrm{d}}[k]-T_{\mathrm{s}}\frac{dI_{\mathrm{d}}[k]}{dt}\right)^2\\&+\left(I_{\mathrm{q}}^*[k]-I_{\mathrm{q}}[k]-T_{\mathrm{s}}\frac{dI_{\mathrm{q}}[k]}{dt}\right)^2\end{aligned} \quad (15)$$

Further, the expression of (15) can be expanded by using (1),

$$\begin{aligned}J=&\left(I_{\mathrm{d}}^*[k]-I_{\mathrm{d}}[k]-\frac{T_{\mathrm{s}}}{L_{\mathrm{g}}}(V_{\mathrm{d}}-E_{\mathrm{d}}-R_{\mathrm{g}}I_{\mathrm{d}}[k]+w_{\mathrm{s}}L_{\mathrm{g}}I_{\mathrm{q}}[k])\right)^2\\&+\left(I_{\mathrm{q}}^*[k]-I_{\mathrm{q}}[k]-\frac{T_{\mathrm{s}}}{L_{\mathrm{g}}}(V_{\mathrm{q}}-E_{\mathrm{q}}-R_{\mathrm{g}}I_{\mathrm{q}}[k]-w_{\mathrm{s}}L_{\mathrm{g}}I_{\mathrm{d}}[k])\right)^2\end{aligned} \quad (16)$$

It is noted that (16) is a multivariable function by variables $\boldsymbol{v}^{\mathrm{dq}}=[V_{\mathrm{d}},\ V_{\mathrm{q}}]^{\mathrm{T}}$ which vary with the selection of the switching state in (3). In order to derive the minima of (16), (16) is first treated to be the function with the continuous variable domain, and variables $[V_{\mathrm{d}},\ V_{\mathrm{q}}]^{\mathrm{T}}$ are both continuous real-valued variables. For a continuous multivariable function, these equations below need to be held to derive the minima,

This article has been accepted for publication in a future issue of this journal, but has not been fully edited. Content may change prior to final publication. Citation information: DOI 10.1109/OJIA.2021.3091154, IEEE Open Journal of Industry Applications

$$\nabla J = \begin{bmatrix} \dfrac{dJ}{dV_{\mathrm{d}}} \\ \dfrac{dJ}{dV_{\mathrm{q}}} \end{bmatrix} = \vec{0} \tag{17}$$

and

$$\begin{cases} D = \dfrac{d^2J}{dV_{\mathrm{d}}^2} \cdot \dfrac{d^2J}{dV_{\mathrm{q}}^2} - \left(\dfrac{d^2J}{dV_{\mathrm{d}}dV_{\mathrm{q}}}\right)^2 > 0 \\ \dfrac{d^2J}{dV_{\mathrm{d}}^2} > 0, \ \dfrac{d^2J}{dV_{\mathrm{q}}^2} > 0 \end{cases} \tag{18}$$

Then, (17) and (18) are calculated and the results are below,

$$\nabla J = -2\frac{T_{\mathrm{s}}}{L_{\mathrm{g}}} \begin{bmatrix} I_{\mathrm{d}}^*[k] - I_{\mathrm{d}}[k] - \dfrac{T_{\mathrm{s}}}{L_{\mathrm{g}}}(V_{\mathrm{d}} - E_{\mathrm{d}} - R_{\mathrm{g}}I_{\mathrm{d}}[k] + w_{\mathrm{s}}L_{\mathrm{g}}I_{\mathrm{q}}[k]) \\ I_{\mathrm{q}}^*[k] - I_{\mathrm{q}}[k] - \dfrac{T_{\mathrm{s}}}{L_{\mathrm{g}}}(V_{\mathrm{q}} - E_{\mathrm{q}} - R_{\mathrm{g}}I_{\mathrm{q}}[k] - w_{\mathrm{s}}L_{\mathrm{g}}I_{\mathrm{d}}[k]) \end{bmatrix} \tag{19}$$

and

$$\begin{cases} D = 4\left(\dfrac{T_{\mathrm{s}}}{L_{\mathrm{g}}}\right)^4 \\ \dfrac{d^2J}{dV_{\mathrm{d}}^2} = 2\left(\dfrac{T_{\mathrm{s}}}{L_{\mathrm{g}}}\right)^2, \ \dfrac{d^2J}{dV_{\mathrm{q}}^2} = 2\left(\dfrac{T_{\mathrm{s}}}{L_{\mathrm{g}}}\right)^2 \end{cases} \tag{20}$$

Equation (20) shows itself permanently greater than zero by positive T_{s} and L_{g}, whereas any $\boldsymbol{v}^{\mathrm{dq}} = [V_{\mathrm{d}}, V_{\mathrm{q}}]^{\mathrm{T}}$ leading to a zero-vector equality in (17) will perform a minimum of (16).

Then, (16) is treated to be the function with the limited domain as its actual situation, and variables $[V_{\mathrm{d}}, V_{\mathrm{q}}]^{\mathrm{T}}$ are both piecewise constant variables according to the finite number of switching states. (17) is downgraded to (21) below for a minimum. In this case, any input $\boldsymbol{v}^{\mathrm{dq}}$ which drives the gradient ∇J (19) closest to the zero vector will perform a local minimum point of the multivariable function (16).

$$\min_{\boldsymbol{v}^{\mathrm{dq}}} \left\| \nabla J - \vec{0} \right\|_2 \tag{21}$$

Further, in the system steady state, the instantaneous current $\boldsymbol{i}^{\mathrm{dq}}[k]$ is very close to its reference, $\boldsymbol{i}^{\mathrm{dq}*}[k]$, which can be approximated to be identical for the ideal case, $\boldsymbol{i}^{\mathrm{dq}}[k] = \boldsymbol{i}^{\mathrm{dq}*}[k]$, Then, (19) can be simplified into the following,

$$\nabla J = -2\frac{T_{\mathrm{s}}}{L_{\mathrm{g}}} \begin{bmatrix} -\dfrac{T_{\mathrm{s}}}{L_{\mathrm{g}}}(V_{\mathrm{d}} - E_{\mathrm{d}} - R_{\mathrm{g}}I_{\mathrm{d}}^*[k] + w_{\mathrm{s}}L_{\mathrm{g}}I_{\mathrm{q}}^*[k]) \\ -\dfrac{T_{\mathrm{s}}}{L_{\mathrm{g}}}(V_{\mathrm{q}} - E_{\mathrm{q}} - R_{\mathrm{g}}I_{\mathrm{q}}^*[k] - w_{\mathrm{s}}L_{\mathrm{g}}I_{\mathrm{d}}^*[k]) \end{bmatrix} \tag{22}$$

Combining (21) and (22) together, the optimal solution of the objective function (16) can also be derived through solving the following optimization problem. Their optimal solutions are equivalent through (17)-(22), even though their optimal values are not the same.

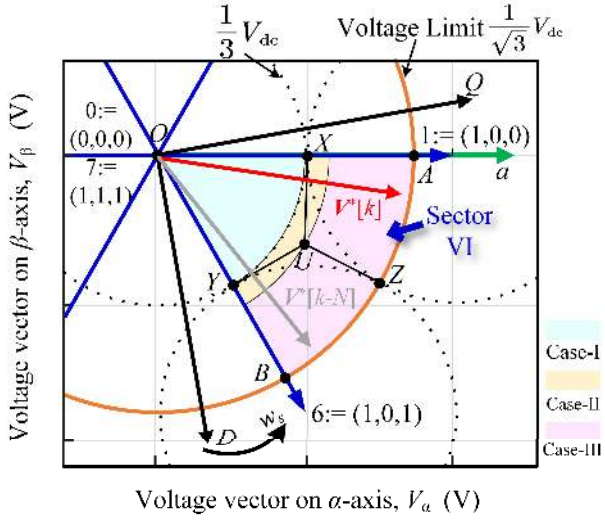

Fig. 2 Schematic diagram of the ideal case switching state in Sector VI on the voltage vector space with both *abc* (green) and *dq* (black) frames.

$$\min_{\boldsymbol{v}^{\mathrm{dq}}} \left\| 2\left(\frac{T_s}{L_g}\right)^2 \begin{bmatrix} (V_{\mathrm{d}} - V_{\mathrm{d}}^*[k]) \\ (V_{\mathrm{q}} - V_{\mathrm{q}}^*[k]) \end{bmatrix} - \vec{0} \right\|_2 \tag{23}$$

where

$$\begin{cases} V_{\mathrm{d}}^*[k] = E_{\mathrm{d}} + R_{\mathrm{g}}I_{\mathrm{d}}^*[k] - w_{\mathrm{s}}L_{\mathrm{g}}I_{\mathrm{q}}^*[k] \\ V_{\mathrm{q}}^*[k] = E_{\mathrm{q}} + R_{\mathrm{g}}I_{\mathrm{q}}^*[k] + w_{\mathrm{s}}L_{\mathrm{g}}I_{\mathrm{d}}^*[k] \end{cases} \tag{24}$$

$\boldsymbol{v}^{\mathrm{dq}*} = [V_{\mathrm{d}}^*, V_{\mathrm{q}}^*]^{\mathrm{T}} \in \mathbb{R}^{2\mathrm{x}1}$ represents the converter output voltage reference from the command. At this point, it is observed that finding a local minimum of (16) is equivalent to seek for an input $\boldsymbol{v}^{\mathrm{dq}}$ that leads to a minimized distance between the reference $\boldsymbol{v}^{\mathrm{dq}*}$ and this input $\boldsymbol{v}^{\mathrm{dq}}$ in (23). Then, the switching state of this input becomes the optimum. With multiple iterations of FCS-MPC, the switching sequence will be determined by this algorithm.

C. Switching Sequence Analysis with $\boldsymbol{i}^{\mathrm{dq}}[\mathrm{k}] = \boldsymbol{i}^{\mathrm{dq}*}[\mathrm{k}]$

Fig. 2 shows a zoom-in area of the voltage vector space for the two-level power converter. It contains the stationary *abc* reference frame (green) and the rotating *dq* reference frame (black) at the same origin *O*. It displays an output voltage reference $\boldsymbol{V}^*$, as an example, rotating at the speed w_{s} and is temporarily located in Sector VI which is the region *OAB* constituted by voltage vectors of non-zero switching states $\boldsymbol{s}_1{}^{\mathrm{abc}} = (1,0,0)$, $\boldsymbol{s}_6{}^{\mathrm{abc}} = (1,0,1)$ and the voltage limit curve $V_{\mathrm{dc}}/\sqrt{3}$.

As mentioned above, the optimal switching state is the one of which the voltage vector has the minimized distance to the output voltage reference. Based on this discovery, the region *OAB* is further divided into three quadrilateral subareas, *OXUY*, *AZUX*, *BYUZ*, which are partitioned by included points having the shortest distance to the voltage vectors of $\boldsymbol{s}_{0/7}{}^{\mathrm{abc}}$, $\boldsymbol{s}_1{}^{\mathrm{abc}}$, and $\boldsymbol{s}_6{}^{\mathrm{abc}}$, respectively. *X* and *Y* are the middle points of voltage vectors of $\boldsymbol{s}_1{}^{\mathrm{abc}}$ and $\boldsymbol{s}_6{}^{\mathrm{abc}}$. *Z* is the middle point of the curve *AB*. The length of *OX* or *OY* is $V_{\mathrm{dc}}/3$. *U* is the center of the inscribed circle of Sector VI. The length of *OU* is $2V_{\mathrm{dc}}/3\sqrt{3}$. It is illustrated graphically that the optimal switching states will be $\boldsymbol{s}_{0/7}{}^{\mathrm{abc}}$, $\boldsymbol{s}_1{}^{\mathrm{abc}}$, and $\boldsymbol{s}_6{}^{\mathrm{abc}}$ for any output

This article has been accepted for publication in a future issue of this journal, but has not been fully edited. Content may change prior to final publication. Citation information: DOI 10.1109/OJIA.2021.3091154, IEEE Open Journal of Industry Applications

voltage references located at *OXUY*, *AZUX*, and *BYUZ*, respectively. Hence, for the reference $\boldsymbol{V}^*$ shown in Fig. 2, the selected optimal switching state by FCS-MPC will be $\boldsymbol{s}_1^{abc}$.

Besides, this output voltage reference is not stationary but rotating at w_s. $\boldsymbol{V}^*[k\text{-}N]$ which is $\boldsymbol{V}^*$ in N discrete time instants earlier will have an optimal switching state at $\boldsymbol{s}_6^{abc}$ since $\boldsymbol{V}^*[k\text{-}N]$ was in *BYUZ* at that time instead of *AZUX*, as shown in Fig. 2. It is quite complicated if $\boldsymbol{V}^*$ has a magnitude greater than $V_{dc}/3$ and smaller than $2V_{dc}/3\sqrt{3}$. It will locate at *BYUZ*, *OXUY* and *AZUX* in succession, which gives the optimal switching state in a sequence of $\boldsymbol{s}_6^{abc}$, $\boldsymbol{s}_{0/7}^{abc}$, and $\boldsymbol{s}_1^{abc}$.

Therefore, for an output voltage reference $\boldsymbol{V}^*$, the ideal sequence of the optimal switching states will be provided below:

For Case-I, $\|\boldsymbol{V}^*\|_2 <= V_{dc}/3$,

$$\rightarrow \boldsymbol{s}_{0/7}^{abc} \rightarrow\ldots\rightarrow \boldsymbol{s}_{0/7}^{abc} \rightarrow\ldots\rightarrow$$

For Case-II, $\|\boldsymbol{V}^*\|_2 > V_{dc}/3$ and $\|\boldsymbol{V}^*\|_2 < 2V_{dc}/3\sqrt{3}$,

$$\rightarrow \boldsymbol{s}_6^{abc} \rightarrow\ldots\rightarrow \boldsymbol{s}_{0/7}^{abc} \rightarrow\ldots\rightarrow \boldsymbol{s}_1^{abc} \rightarrow\ldots\rightarrow$$

For Case-III, $\|\boldsymbol{V}^*\|_2 >= 2V_{dc}/3\sqrt{3}$,

$$\rightarrow \boldsymbol{s}_6^{abc} \rightarrow\ldots\rightarrow \boldsymbol{s}_1^{abc} \rightarrow\ldots\rightarrow$$

where … represents that the current switching state is the same as the last one. For example, "→ $\boldsymbol{s}_6^{abc}$ →…→" is equivalent to "→ $\boldsymbol{s}_6^{abc}$ → $\boldsymbol{s}_6^{abc}$→ $\boldsymbol{s}_6^{abc}$ → $\boldsymbol{s}_6^{abc}$ →" as long as $\boldsymbol{V}^*$ rotates in *BYUZ*. According to above different switching sequences, it is noted that Case-I could have the smallest switching frequency since its sequence is either all $\boldsymbol{s}_0^{abc}$ or all $\boldsymbol{s}_7^{abc}$. Case-II has a sequence with both non-zero and zero switching states. Case-III has a sequence with only non-zero switching states.

D. Switching Sequence Analysis with $\boldsymbol{i}^{dq}[k] \neq \boldsymbol{i}^{dq^*}[k]$

Then, the nonideal case is analyzed, where the assumption made for (22) does not always hold, $\boldsymbol{i}^{dq}[k] \neq \boldsymbol{i}^{dq^*}[k]$. In the real system, there is an instantaneous current error between $\boldsymbol{i}^{dq}[k]$ and $\boldsymbol{i}^{dq^*}[k]$. Even if the selected optimal switching state from (23) has the minimized distance to the output voltage reference, it does not lead to a zero-vector equality in (17), which results in a voltage vector error and thereby the instantaneous current error. A more sophisticated equation of (23) can be written by involving this error,

$$\min_{\boldsymbol{v}^{dq}} \left\| 2\left(\frac{T_s}{L_g}\right)^2 \left[\begin{pmatrix} V_d - \left(V_d^*[k] + \sum_{j=0}^{N} V_d^C[k-j] \right) \\ V_q - \left(V_q^*[k] + \sum_{j=0}^{N} V_q^C[k-j] \right) \end{pmatrix} \right] - \vec{0} \right\|_2 \quad (25)$$

where $\boldsymbol{V}^C := \boldsymbol{v}^{dqC} = [V_d^C, V_q^C]^T \in \mathbb{R}^{2x1}$ is the output voltage compensation in order to compensate the instantaneous current error from previous time instants. With the error aggregates, $\boldsymbol{V}^C$ would take up more weightings in the vector sum of $\boldsymbol{V}^C$ and $\boldsymbol{V}^{dq^*}$, and eventually lead the vector sum to another quadrilateral subarea.

In Fig. 3, $\boldsymbol{V}^C$ is the output voltage compensation for the output voltage reference $\boldsymbol{V}^*$ in the k instant. Assume the ideal

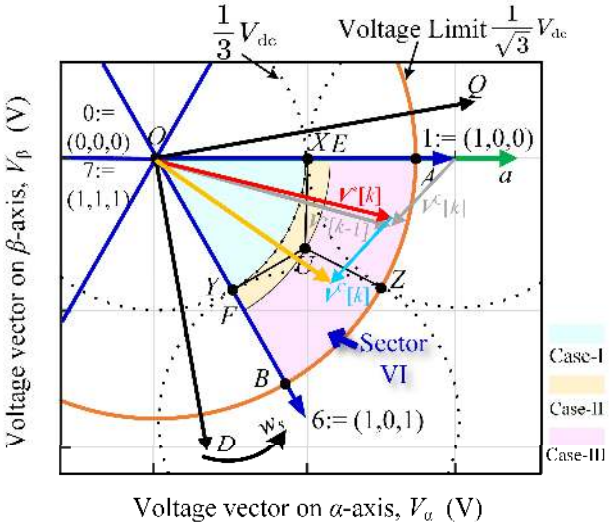

Fig. 3 Schematic diagram of nonideal case switching state in Sector VI on the voltage vector space with both *abc* (green) and *dq* (black) frames.

case holds before the k-1 instant, $\boldsymbol{V}^C$ is also the voltage vector error by the selected optimal switching state $\boldsymbol{s}_1^{abc}$ in the k-1 instant. Hence, from (25), the optimal switching state is selected for the k instant based on the superposition of the $\boldsymbol{V}^*$ and $\boldsymbol{V}^C$, which is shown in yellow in Fig. 3. At this point, the optimal switching state is $\boldsymbol{s}_6^{abc}$ since the vector sum of $\boldsymbol{V}^*$ and $\boldsymbol{V}^C$ slides into *BYUZ* instead of *AZUX*. Extending this nonideal analysis into all three cases, the switching sequence will be updated into the following,

For Case-I, $\|\boldsymbol{V}^*\|_2 <= V_{dc}/3$,

$$\rightarrow \boldsymbol{s}_{0/7}^{abc} \rightarrow\ldots\rightarrow \boldsymbol{s}_{1/6}^{abc} \rightarrow \boldsymbol{s}_{0/7}^{abc} \rightarrow\ldots\rightarrow \boldsymbol{s}_{1/6}^{abc} \rightarrow \boldsymbol{s}_{0/7}^{abc} \rightarrow\ldots\rightarrow$$

For Case-II, $\|\boldsymbol{V}^*\|_2 > V_{dc}/3$ and $\|\boldsymbol{V}^*\|_2 < 2V_{dc}/3\sqrt{3}$,

$$\rightarrow \boldsymbol{s}_6^{abc} \rightarrow\ldots\rightarrow \boldsymbol{s}_{0/7}^{abc} \rightarrow \boldsymbol{s}_6^{abc} \rightarrow\ldots\rightarrow \boldsymbol{s}_{0/7}^{abc} \rightarrow\ldots\rightarrow \boldsymbol{s}_{1/6}^{abc} \rightarrow \boldsymbol{s}_{0/7}^{abc} \rightarrow\ldots\rightarrow \boldsymbol{s}_1^{abc} \rightarrow\ldots\rightarrow \boldsymbol{s}_{0/7}^{abc} \rightarrow \boldsymbol{s}_1^{abc} \rightarrow\ldots\rightarrow$$

For Case-III, $\|\boldsymbol{V}^*\|_2 >= 2V_{dc}/3\sqrt{3}$,

$$\rightarrow \boldsymbol{s}_6^{abc} \rightarrow\ldots\rightarrow \boldsymbol{s}_{0/7}^{abc} \rightarrow \boldsymbol{s}_6^{abc} \rightarrow\ldots\rightarrow \boldsymbol{s}_{0/7}^{abc} \rightarrow \boldsymbol{s}_1^{abc} \rightarrow\ldots\rightarrow$$

It is noted that switching transitions for all cases increase due to voltage compensations. These increased transitions will induce an increased switching frequency over the fundamental period. For instance, Case-I has more switching transitions from non-zero switching states, $\boldsymbol{s}_6^{abc}$ or $\boldsymbol{s}_1^{abc}$ ($\boldsymbol{s}_{1/6}^{abc}$), and results in a higher switching frequency. Case-II becomes more complicated. When $\boldsymbol{V}^*$ rotates into *FYU* area, $\boldsymbol{s}_{0/7}^{abc}$ is used to compensate the voltage error from the ideal case results $\boldsymbol{s}_6^{abc}$. Similarly, $\boldsymbol{s}_6^{abc}$ or $\boldsymbol{s}_1^{abc}$ ($\boldsymbol{s}_{1/6}^{abc}$) appears to compensate the voltage error for *XUY* area and $\boldsymbol{s}_{0/7}^{abc}$ is applied again to compensate the voltage error for *EUX* area, where this switching sequence accords with the real system.

At this moment, the switching frequency variation can be investigated by analyzing the potential number of switching transitions within each case and comparing the boundary conditions between all three cases.

In Case-I, an output voltage reference $\boldsymbol{V}^*$ with a smaller magnitude would contribute to a smaller voltage vector error by $\boldsymbol{s}_{0/7}{}^{abc}$ and need more aggregations driving the sum of $\boldsymbol{V}^*$ and $\boldsymbol{V}^C$ to the different subarea. Hence, this $\boldsymbol{V}^*$ requires fewer transitions from non-zero switching states for the voltage compensation. Then, its switching frequency will be less than the $\boldsymbol{V}^*$ with a larger magnitude. The maximum switching frequency happens when $\boldsymbol{V}^*$ is located at the boundary of Case-I which is the $V_{dc}/3$ curve. In Case-III, on the contrary, the switching frequency will gradually increase while the magnitude of $\boldsymbol{V}^*$ decreases. The similar analysis can be applied here. The maximum switching frequency happens when $\boldsymbol{V}^*$ is located at the boundary of Case-III which is $2V_{dc}/3\sqrt{3}$.

Even though switching sequences in Case-II are more complicated than other two cases, it still can be inferred that the switching frequency will increase while the magnitude of the output voltage reference $\boldsymbol{V}^*$ decreases. This is because $\boldsymbol{V}^*$ with a smaller magnitude in Case-II would move along a longer curve located in *OXUY*. A longer curve in *OXUY* could trigger more compensations from non-zero switching states like Case-I. One compensation from non-zero switching states may result in two switching transitions, such as $\boldsymbol{s}_0{}^{abc}:=[0,0,0]^T \rightarrow \boldsymbol{s}_6{}^{abc}:=[1,0,1]^T$. However, compensations from zero switching states like Case-III can guarantee that at most one switching transition happens, such as $\boldsymbol{s}_6{}^{abc}:=[1,0,1]^T \rightarrow \boldsymbol{s}_7{}^{abc}:=[1,1,1]^T$ or $\boldsymbol{s}_1{}^{abc}:=[1,0,0]^T \rightarrow \boldsymbol{s}_0{}^{abc}:=[0,0,0]^T$, since $\boldsymbol{s}_7{}^{abc}$ and $\boldsymbol{s}_7{}^{abc}$ are replaceable in terms of the output voltage vector. Hence, $\boldsymbol{V}^*$ in Case-II which moves along a longer curve in *OXUY* will generate more switching transitions due to compensations from non-zero switching states, eventually a higher switching frequency. The maximum switching frequency happens when $\boldsymbol{V}^*$ is located at the inner boundary of *OXUY* which is the $V_{dc}/3$ curve.

E. Summary of Variable Switching Frequency Property

Combining the switching frequency variations in all three cases, it is illustrated that the maximum switching frequency of the basic problem formulation happens when $\boldsymbol{V}^*$ has a magnitude around the $V_{dc}/3$ curve and the switching frequency decreases in both directions that the magnitude of $\boldsymbol{V}^*$ increases or decreases away from the $V_{dc}/3$ curve. Besides, the phase of $\boldsymbol{V}^*$ in the *dq* reference frame would not affect the switching frequency since the *dq* reference frame is rotating at the speed w_s and it will sweep full degrees in the *abc* reference frame, which is always true regardless of the voltage phase. To put everything in a nutshell, the variable switching frequency property of FCS-MPC can be summarized in the following:

1) The optimal switching state can be decided by selecting the switching state of which the voltage vector has the minimized distance to the output voltage reference, if the instantaneous current is assumed to be the same as reference.
2) In the real situation, where there is an instantaneous current error, the optimal switching state can be decided by selecting the switching state of which the voltage vector has the minimized distance to the vector sum of the output voltage reference and the voltage compensation.
3) The maximum switching frequency happens when the output voltage reference $\boldsymbol{V}^*$ has a magnitude around $V_{dc}/3$.
4) The switching frequency decreases in both directions that the magnitude of $\boldsymbol{V}^*$ increases or decreases away from $V_{dc}/3$.
5) The voltage phase of $\boldsymbol{V}^*$ in the *dq* rotating reference frame would not affect the switching frequency.

The value quantization of the switching frequency in FCS-MPC is complex and out of scope of this paper. The above proposed principles are significant enough to comprehend the control algorithms of FCS-MPC and provide engineers with more insights to fully leverage the FCS-MPC.

III. Feasible Operation Range of GCI

In this section, the feasible operation range of the power converter is described in order to verify the switching frequency variation property of FCS-MPC for different steady states of the GCI. As inferred in Section II, the switching frequency varies with the magnitude of the output voltage reference $\boldsymbol{V}^*$. The $\boldsymbol{V}^*$ is actually determined by power flow control as shown in Fig. 1 and generated by $\boldsymbol{i}^{dq*}$ in (24). In this case, if the magnitudes of $\boldsymbol{V}^*$ for all feasible steady states are estimated, the switching frequency variation can be tracked for the FCS-MPC regulated power converter. Hence, the first task is to identify all feasible steady states of the power converter. This is exactly the feasible operation range in the voltage vector space. Each operating point in this range is one potential steady state of GCI.

A 1-MVA grid-connected inverter is introduced from the reference model of the ocean current energy converter (OCEC) system as a description example [45]. The system parameters of this GCI are listed in Table I, where the DC bus voltage and line reactors are selected for the purpose of more simulation validations. Six ABB HiPak 5SND 0800M170100 IGBT modules [46] are used for this two-level three-phase topology as shown in Fig. 1, and each module has two paralleled same-polarity IGBT devices with diodes to increase current loadings.

Fig. 4 presents the complete voltage vector space for the two-level power converter. Both *abc* stationary and *dq* rotating reference frames are shown in Fig. 4. Voltage vectors of eight switching states from (3) and (4) are displayed in blue. The output voltage limit of FCS-MPC regulated GCI is specified in,

$$\sqrt{V_d^2+V_q^2} \leqslant V_{dc}/\sqrt{3} \tag{26}$$

This contours the maximal linear modulation region in the voltage vector space. The overmodulation operation of FCS-MPC [20] requires the switching penalty objective function and is not concerned in this paper. The current limit curve is expressed as,

$$\sqrt{I_d^2+I_q^2} \leqslant I_{limit} \tag{27}$$

Then, (27) is mapped into the voltage vector space as,

$$\frac{(V_d-E_d)^2}{(w_s L_g I_{limit})^2}+\frac{(V_q-E_q)^2}{(w_s L_g I_{limit})^2} \leqslant 1 \tag{28}$$

This article has been accepted for publication in a future issue of this journal, but has not been fully edited. Content may change prior to final publication. Citation information: DOI 10.1109/OJIA.2021.3091154, IEEE Open Journal of Industry Applications

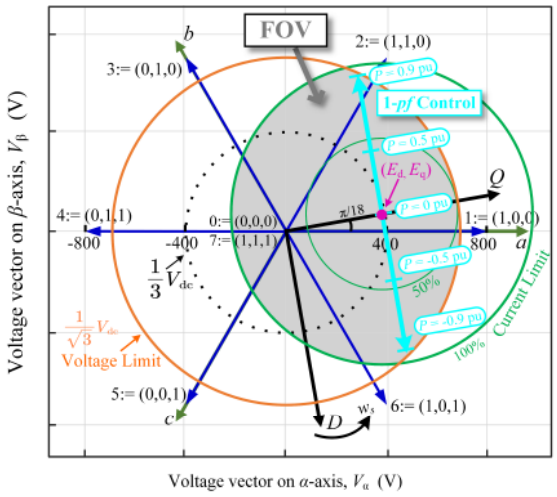

Fig. 4 Feasible operation range of GCI in the voltage vector space.

TABLE I
PARAMETERS OF THE GCI IN THE REFERENCE OCEC SYSTEM

Rated power S	1 MVA/ 1 p.u.
Rated DC bus voltage V_{dc}	1200 V
Grid frequency f_g	60 Hz
Rated AC grid voltage e^{abc}	277/480 V
Line inductance L_g	1 mH
Line resistance R_g	10 mΩ
IGBT module	ABB HiPak 5SND0800M170100 [46]
Junction temperature T_j	-40~125 ºC, Max 150 ºC
Air temperature T_{air}	25 ºC
50% current loading	601.7 A
100% current loading (rated)	1203.4 A

Details of derivation are in Appendix. I_{limit} could be either the maximum continuous conduction current of the semiconductor device or the power derating limit. In this example, I_{limit} is 100% current loading of the 1-MVA system.

The intersection of interior areas of voltage and current limits (26) and (28) is the feasible operation range of this GCI in the voltage vector space (FOV), which is indicated in shadow in Fig. 4. By different current loading limits, the intersection area varies. 50% derating and 100% 1-MVA current loadings are both shown in Fig. 4 in green, which illustrates different feasible operation ranges. The $V_{dc}/3$ curve is shown in the dash line by

$$\sqrt{V_d^2 + V_q^2} = V_{dc}/3 \tag{29}$$

Any operating point in the shadow is one potential steady state of this GCI. Any operating point located around the $V_{dc}/3$ curve will have a larger switching frequency by FCS-MPC and the switching frequency decreases with the operating point moving away from this curve, as inferred in Section II.

The most conventional power flow control is the unity power factor (1-*pf*) control shown in blue in Fig. 4 for DER systems. The FCS-MPC controlled GCI will perform different switching frequencies along this control trajectory because of different distances from the operating point to the $V_{dc}/3$ curve. It is also observed that by injecting an amount of the reactive power, the switching frequency will be autonomously adjusted since the operating point is moving closer to or further away from the $V_{dc}/3$ curve. The following sections will verify this variable switching frequency property of FCS-MPC in FOV.

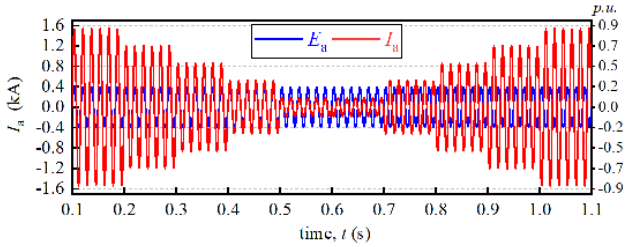

Fig. 5. Simulation results of the unity power factor control by FCS-MPC (base: line current peak 1701 A).

TABLE II
PARAMETERS OF THE FCS-MPC WITH BASIC PROBLEM FORMULATION

Prediction receding horizon H	1
Sampling period T_s	50 µs

IV. SIMULATION RESULTS

To verify the variable switching frequency property of the FCS-MPC and other discoveries discussed above, PLECS and MATLAB/Simulink software tools are used to simulate the sample 1-MVA GCI, considering the system diagram in Fig. 1. FCS-MPC with the basic problem formulation (10)-(13) is calibrated on the local controller. The parameters are set and listed in Table II. The 50-µs sampling time T_s is selected for a typical low switching frequency level in the MVA-scale application due to the significant switching loss with the high power semiconductor devices. FOV of this simulated GCI is the same as illustrated in Fig. 4.

Fig. 5 presents the results under 1-*pf*, where grid voltage and current are shown. The reactive power is regulated to be zero and the real power is controlled ranging from 0.9 p.u. to -0.9 p.u., which is following the 1-*pf* trajectory in Fig. 4. The grid voltage and current are presented in phase and 180° out of phase in the inverter and rectifier modes, respectively.

Fig. 6 shows the output switching states by FCS-MPC from 1-*pf* results in Fig. 5. Some operating points, 0.1 p.u. and -0.1 p.u. in Case-I, 0.3 p.u. and -0.3 p.u. in Case-II, and 0.9 p.u. and -0.9 p.u. in Case-III, are presented. It is noted that with the operating point moving towards the $V_{dc}/3$ curve as shown in Fig. 4, from 0.9 p.u. to 0.1 p.u. or from -0.9 p.u. to -0.1 p.u., switching transitions become more frequent. The loci of operating points 0.1 p.u. and -0.1 p.u. in Fig. 6(a) and (d) are closer to the $V_{dc}/3$ curve than the loci of operating points 0.3 p.u. and -0.3 p.u. in Fig. 6(b) and (c), switching transitions appear a little bit more in Fig. 6(a) and (d). Besides, switching sequences of the symmetric operating points are similar, such as 0.9 p.u. and -0.9 p.u., even though they have different $\boldsymbol{V}^*$ phases in *dq* reference frame.

This article has been accepted for publication in a future issue of this journal, but has not been fully edited. Content may change prior to final publication. Citation information: DOI 10.1109/OJIA.2021.3091154, IEEE Open Journal of Industry Applications

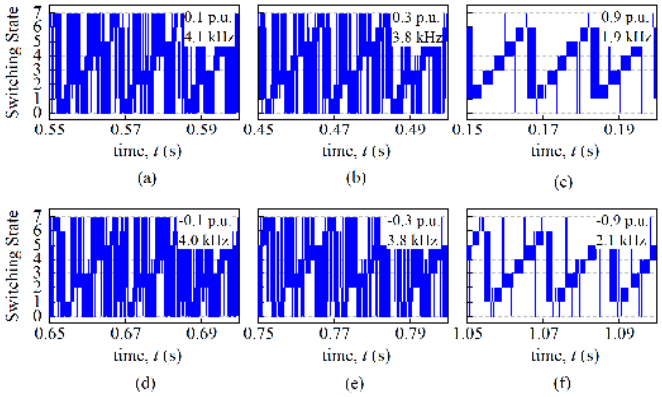

Fig. 6 Output switching states selected by FCS-MPC under 1-*pf*.

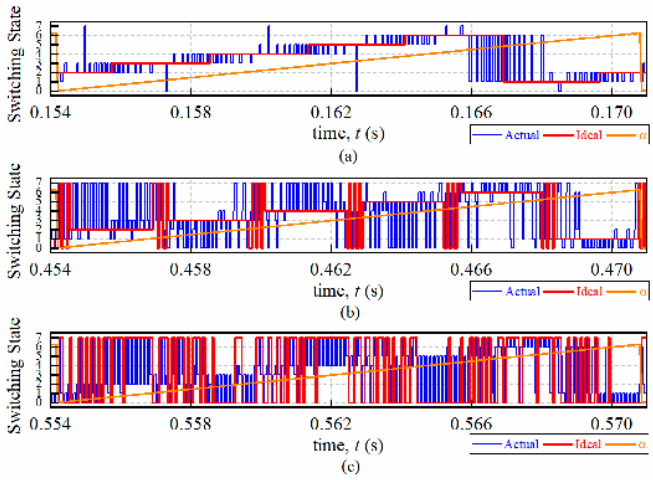

Fig. 7 One fundamental period window of the output switching state by FCS-MPC (blue), the ideal switching sequence by geometry analysis (red), and the rotating angle α of *dq* reference frame (yellow) including (a) 0.9 p.u., (b) 0.3 p.u., and (c) 0.1 p.u..

Fig. 7 shows the zoom-in observations of Fig. 6 over one fundamental period. α is defined as the rotating angle between *dq* and *abc* reference frames. α is π/18 rad in Fig. 4 for instance. Ideal output switching states selected through (23) and (24) are presented in red in addition to the actual output switching states by FCS-MPC in blue. It is found that the results of ideal cases (in red) strictly obey the proposed switching sequences in Section II-C that Case-I only contains zero switching states $\boldsymbol{s}_{0/7}^{abc}$, Case-II contains non-zero switching states $\boldsymbol{s}_{0\text{-}6}^{abc}$ and zero switching states $\boldsymbol{s}_{0/7}^{abc}$, and Case-III only contains non-zero switching states $\boldsymbol{s}_{0\text{-}6}^{abc}$, where the validity of the ideal case inference is verified. Then, nonideal cases (in blue) which are actual switching sequences by close-loop control follow the outlines of ideal cases, but with more transitions due to the current error and the output voltage compensation as discussed in Section II-D. In Fig. 7(a), transitions happen least and are between non-zero switching states $\boldsymbol{s}_{0\text{-}6}^{abc}$, because this operating point is near the outer boundary of FOV. In Fig. 7(b), where the operating point is located in Case-II, transitions happen more from the zero switching states $\boldsymbol{s}_{0/7}^{abc}$ due to the voltage compensation from the zero voltage vector. On the contrary, in Fig. 7(c), transitions happen more from the non-zero

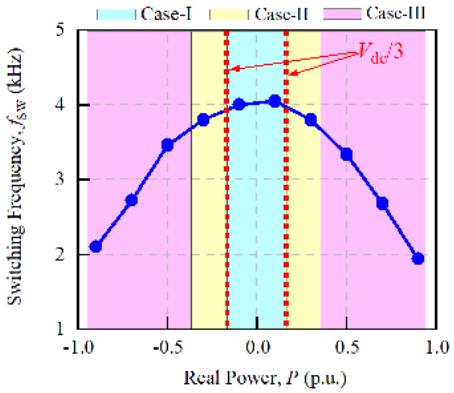

Fig. 8 Switching frequency by FCS-MPC on the 1-*pf* trajectory.

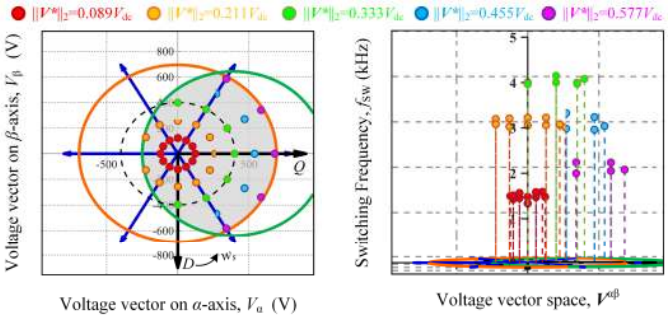

Fig. 9 Switching frequency off the 1-*pf* trajectory (a) loci of operating points on the FOV and (b) corresponding switching frequencies.

switching states $\boldsymbol{s}_{0\text{-}6}^{abc}$ based on the outline of the zero switching states in Case-I. Fig. 7 effectively justifies the proposed switching sequences for both ideal and nonideal cases in Section II.

Then, the switching frequency f_{SW} is calculated by counting the average number of switching transitions in each phase over the time frame t_F as follows,

$$f_{SW} = \frac{f_{SW,A} + f_{SW,B} + f_{SW,C}}{3} \tag{30}$$

where

$$f_{SW,i} = \frac{\text{number of switching events in } t_F}{t_F},\ i = A, B, C \tag{31}$$

t_F is one second in the simulation. Switching frequencies of this GCI under 1-*pf* by FCS-MPC are presented in Fig. 8, which gives an explicit vision on the variable switching frequency property of FCS-MPC. The switching frequency ranges from 2 kHz to 4 kHz, where the minimum value happens when this GCI operates at the outer boundary of FOV at +/-0.9 p.u., and the maximum value happens around the $V_{dc}/3$ curve at +/-0.1 p.u.. It is illustrated that the switching frequency increases with the decrease of the real power because, from FOV in Fig. 4, a smaller loading on the 1-*pf* trajectory causes a smaller output voltage reference magnitude and a closer distance to the $V_{dc}/3$ curve. It is also observed that the symmetric operating points from FOV have

This article has been accepted for publication in a future issue of this journal, but has not been fully edited. Content may change prior to final publication. Citation information: DOI 10.1109/OJIA.2021.3091154, IEEE Open Journal of Industry Applications

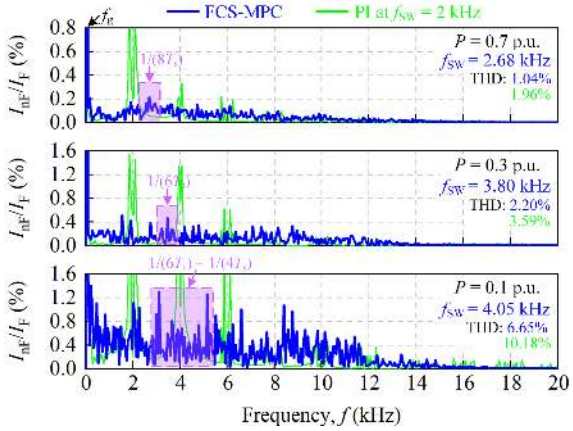

Fig. 10 Frequency spectra of the grid current by FCS-MPC (blue) and conventional PI (green) controllers at P = 0.7, 0.3, and 0.1 p.u..

almost the same switching frequency because of the same output voltage reference magnitude, which indicates that the switching frequency is independent of the output voltage phase. The switching frequency variation in Case-I is not apparent in Fig. 8 due to a very tiny overlap between the 1-*pf* trajectory and the Case-I region in Fig. 4, which will be presented later in results off the 1-*pf* trajectory.

More results of the switching frequency for steady states off the 1-*pf* trajectory are presented in Fig. 9. Several output voltage references $\boldsymbol{V}^*$ with different magnitudes are tested, including $0.577V_{dc}$, $0.455V_{dc}$, $0.333V_{dc}$, $0.211V_{dc}$, and $0.089V_{dc}$. Fig. 9(a) shows loci of the operating points in the FOV, which are grouped by the same output voltage magnitude. It is clear to find in Fig. 9(b) that with the same magnitude of the output voltage reference, switching frequencies of different steady states are at the same level and are independent of the output voltage phase. In addition, the switching frequency is verified to be maximum at 4 kHz around the $V_{dc}/3$ curve, which is the group of the $0.333V_{dc}$ and decreases with the magnitude increasing in groups of $0.455V_{dc}$, and $0.577V_{dc}$, decreases with the magnitude decreasing in groups of $0.211V_{dc}$, and $0.089V_{dc}$.

Then, the impacts of the variable switching frequency on the grid current harmonics and the power loss of semiconductor devices are illustrated in Fig. 10-12. The current harmonics through the FFT analysis by FCS-MPC are compared with the ones by conventional PI control in Fig. 10, where the switching frequency is fixed at 2 kHz in PI control as the system design. It is noted that due to the indefinite switching periods by FCS-MPC, the frequency spectrum spreads over a large frequency range, different from the one centered around the switching frequency and its integer multiples by PI. From the FCS-MPC spectra, it is observed that with the operating point moving towards the $V_{dc}/3$ curve from P = 0.7 p.u. to P = 0.1 p.u., most of the harmonic content shift to the higher orders on the spectrum. For 0.7 p.u., the high-magnitude components exist around the period about eight times of T_s, which results in an average 2.68 kHz switching frequency. For 0.3 p.u., more switching transitions happen due to the current error and the output voltage compensation as discussed in Section II and displayed in Fig. 6 and 7, which shortens the most switching

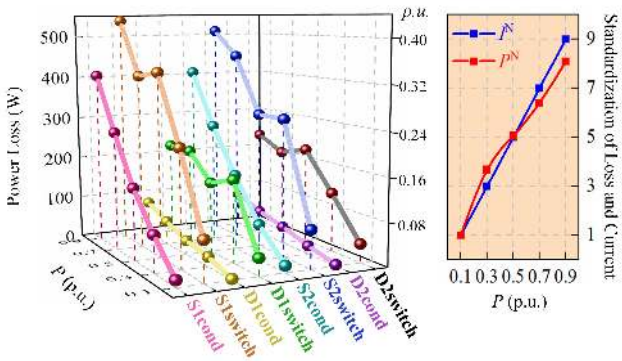

Fig. 11 Loss distribution of one-phase semiconductor devices (S1, D1, S2, and D2) under 1-*pf* trajectory (base: rated single device loss 1250 W).

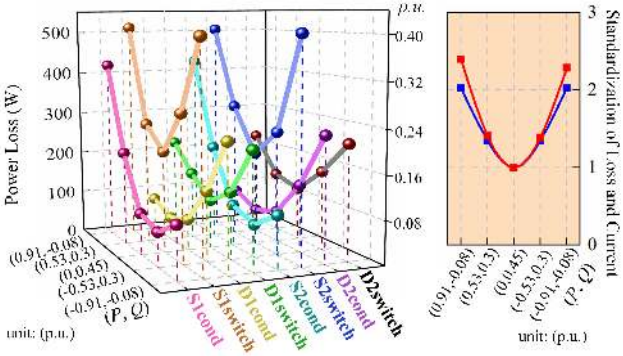

Fig. 12 Loss distribution of one-phase semiconductor devices (S1, D1, S2, and D2) under $0.577V_{dc}$ output voltage magnitude curve (base: rated single device loss 1250 W).

periods from $8T_s$ to $6T_s$, and the switching frequency increases to 3.80 kHz. Further for 0.1 p.u., the switching transitions become even more frequent because the operating point is around the $V_{dc}/3$ curve, and the most switching periods decrease to 4~$6T_s$, which results in an average 4.05 kHz switching frequency. Finally, these harmonics shifts affect the current total harmonics distortion (THD). It is illustrated that THD values at 0.7, 0.3 and 0.1 p.u. are all reduced from 1.96%, 3.59% and 10.18% by PI control to 1.04%, 2.20% and 6.65%, respectively, by FCS-MPC. This is attributed to that high-magnitude components move to the higher orders on the spectrum by FCS-MPC. With the same line reactor, the filter performance will be better with the higher-order components.

Fig. 11 displays the loss distribution of one-phase semiconductor devices (S1, D1, S2, and D2) under 1-*pf*. The temperature dissipation is simulated to guarantee the junction temperature would not exceed 150°C at 1-MVA. All conduction losses vary proportionally with the power loading. However, the switching loss is noticed to be affected by variable switching frequency property significantly. For S1, at 0.5 p.u. loading, its switching loss is even larger than the one at 0.7 p.u. loading. This is because a much higher switching frequency is found at 0.5 p.u. loading in Fig. 8. A similar impact is also discovered for D2 since S1 and D2 are in the complementary conduction path. For 0.3 and 0.1 p.u. loadings, even though switching frequencies keep increasing, due to much lower conduction currents,

This article has been accepted for publication in a future issue of this journal, but has not been fully edited. Content may change prior to final publication. Citation information: DOI 10.1109/OJIA.2021.3091154, IEEE Open Journal of Industry Applications

switching losses decrease. Standardized scales on the one-phase total loss and the conduction current are also indicated. All total losses and conduction currents are divided by values at 0.1 p.u.. In the low power loading, the total loss variation increases with a decreasing slope, resulting from a great reduction on the switching loss. In the high power loading, the total loss variation increases with an increasing slope, which is attributed to a similar switching frequency range, but a much higher current conduction.

Compared with Fig. 11, Fig. 12 displays the loss distribution of one-phase semiconductor devices under the $0.577V_{dc}$ output voltage magnitude curve. As shown in Fig. 9 (purple dots), the switching frequencies for all steady states on this curve are the same around 2 kHz. It is noted that all losses vary with the power loading, and the standardized total loss variation is proportional to the standardized current variation. These findings give an intuitive insight on the loss distribution by FCS-MPC regulated GCI and benefit the loss estimation and the associated thermal management design.

V. Experimental Results

A scale-down GCI prototype is developed to validate the variable switching frequency property of FCS-MPC as shown in Fig. 14. The experimental parameters are shown in Table III, where the 25-μs sampling time T_s is used instead of 50 μs in the simulation because a higher switching frequency level (around 10 kHz) is required in this scale-down GCI prototype to comply with the grid code on the current harmonics and the designed gate drive circuit. The corresponding operating points or steady states of this GCI in FOVs for two types of line reactors (LR) are shown in Fig. 13, respectively. It is noted that with a higher value in LR 2, FOV has a broader area than the one with a lower value. But it may reduce the maximum power loading since the GCI output voltage would drop more on the line reactor.

A. Validations of Variable Switching Frequency Property

Fig. 15 shows the measured GCI phase voltage V_{an}, line current I_a, and grid voltage E_a of the phase A by FCS-MPC. Fig. 15(a)-(d) present waveforms under 1-*pf* with LR 2 at P = 0.4 p.u., 0.5 p.u., 0.6 p.u., and 0.7 p.u. These operating points from 0.4 to 0.7 p.u. are moving away from the $V_{dc}/3$ curve, and the switching frequency is expected to decrease as proposed in Section II. The phase voltage V_{an} reflects the switching states of the phase A by FCS-MPC, where $V_{an} = V_{dc}$ represents the switching state $s^a = 1$ and $V_{an} = 0$ represents the switching state $s^a = 0$. It is observed that with the power loading increasing from 0.4 to 0.7 p.u, the phase voltage V_{an} has the fewer voltage transitions between V_{dc} and zero, which illustrates the fewer switching transitions between 1 and 0. Obviously, the switching frequency over one fundamental period will decrease, which verifies the proposed property.

Fig. 15(e) presents the waveform under 1-*pf* with LR 1 at P = 0.4 p.u. Fig. 15(a) and (e) give the same current loading since they are both controlled at 0.4 p.u. However, the phase voltage V_{an} displays more voltage transitions for LR 1 than the one for LR 2, which reflects more switching transitions for LR 1. This can be explained by the variable switching frequency property of FCS-MPC in Section II, that even though they are under the same power loading, the location of the operating point in FOV is different. LR 1 gives a magnitude of the converter output voltage closer to the $V_{dc}/3$ curve compared to the LR 2 in Fig. 13, where the switching frequency is expected to be higher.

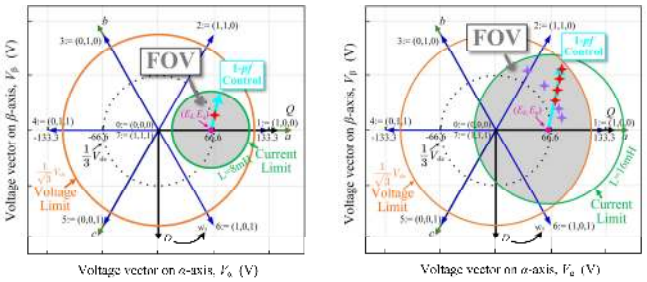

(a) (b)

Fig. 13 Feasible operation ranges for (a) LR 1 and (b) LR 2.

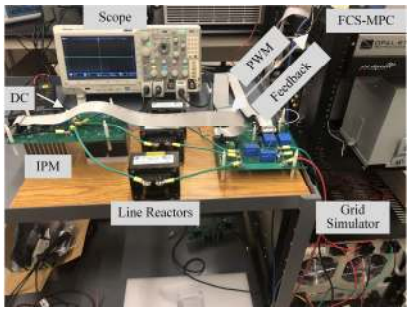

Fig. 14 Experimental prototype of the grid-connected inverter.

TABLE III
Parameters of the GCI in the Experiments

Rated power S	1.4 kVA/ 1 p.u.
Rated DC bus voltage V_{dc}	200 V
Grid frequency f_g	60 Hz
Rated AC grid voltage $\boldsymbol{e}^{abc}$	46.2/80 V
Rated line current $\boldsymbol{i}^{abc}$	10.1 A
Line Reactors 1 L_{g1} R_{g1}	8 mH, 0.3 Ω
Line Reactors 2 L_{g2} R_{g2}	16 mH, 0.5 Ω
IGBT module	Infineon IKCM15L60GD [47]
Sampling period T_s	25 μs

Fig. 15(b) and (f)-(h) presents waveforms with LR 2 at the magnitude of the GCI output voltage reference around $0.4V_{dc}$, i.e., 80V. The phases between E_a and I_a on these four operating points are significantly different. However, the phase voltages V_{an} display about the same amount of the voltage transitions between V_{dc} and zero, which gives about the same amount of the switching transitions. The specific switching frequency values are compared below.

The instantaneous switching frequencies for steady states under 1-*pf* are shown in Fig. 16. Fig. 16(a) and (b) present results for LR 1 and LR 2, respectively. The instantaneous switching frequency is calculated by (30)-(31) with t_F equals to the fundamental period, $1/f_g$. The maximum switching frequency happens for both LR 1 and LR 2 around 10 kHz, which are operating points of low power loadings close to the $V_{dc}/3$ curve from FOVs. It is noted that the collection of

This article has been accepted for publication in a future issue of this journal, but has not been fully edited. Content may change prior to final publication. Citation information: DOI 10.1109/OJIA.2021.3091154, IEEE Open Journal of Industry Applications

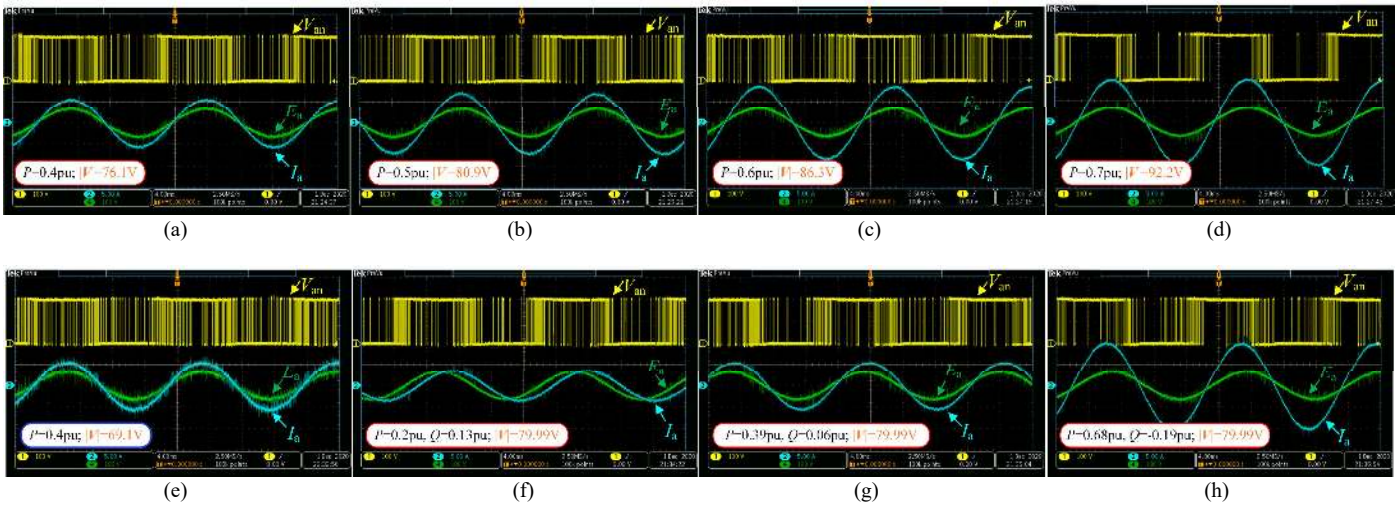

Fig. 15 Experimental results of GCI phase voltage V_{an} (yellow), line current I_a (blue), and grid voltage E_a (green) of the phase A by FCS-MPC including (a) P = 0.4 p.u. with LR 2, (b) P = 0.5 p.u. with LR 2, (c) P = 0.6 p.u. with LR 2, (d) P = 0.7 p.u. with LR 2, (e) P = 0.4 p.u. with LR 1, (f) P = 0.2 p.u. Q = 0.13 p.u. with LR 2, (g) P = 0.39 p.u. Q = 0.06 p.u. with LR 2, (h) P = 0.68 p.u. Q = -0.19 p.u. with LR 2.

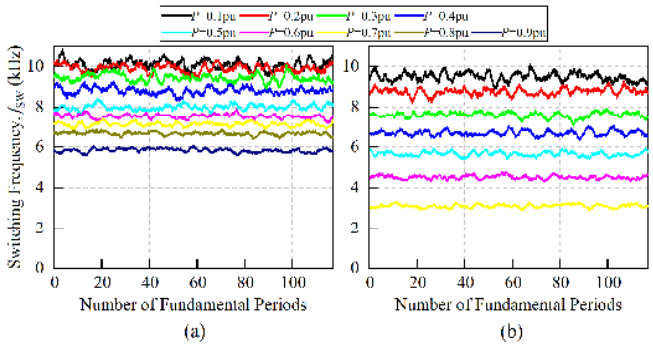

Fig. 16 Instantaneous switching frequency by FCS-MPC under 1-*pf* power trajectory including (a) LR 1 case and (b) LR 2 case.

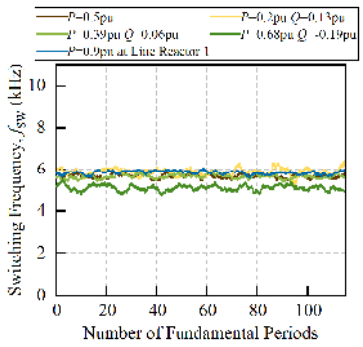

Fig. 17 Instantaneous switching frequency by FCS-MPC under $0.4V_{dc}$ output voltage magnitude curve.

the switching frequency in LR 1 case is higher than the one in LR 2 case. This is because, in LR 1 case, all operating points in FOV are much closer to the $V_{dc}/3$ curve, where it provides the GCI with a higher switching frequency at the same power loading. In LR 2 case, FOV is broader in Fig. 13, where it provides the GCI with an output voltage magnitude further away from the $V_{dc}/3$ curve and eventually a lower switching frequency range.

Another instantaneous switching frequency result is depicted in Fig. 17, where the instantaneous switching frequencies are calculated for experiments from Fig. 15(b) and (f)-(h) and P = 0.9 p.u. in LR 1 case. All of these tests have GCI output voltage magnitudes around $0.4V_{dc}$. It is explicitly illustrated that the switching frequencies are all about the same level, and from 6 kHz to 5.5 kHz. This justifies that the same converter output voltage magnitude contributes to about the same switching frequency and the switching frequency is independent of the phase angle of the output voltage.

By collecting all experiment results and calculating the mean value of the instantaneous switching frequency, the switching frequency distribution over the magnitude of the converter output voltage reference is presented in Fig. 18. Three case regions and the $V_{dc}/3$ curve are identified. It is observed that for the same output voltage magnitude, the switching frequencies for both LR 1 and LR 2 cases turn to be highly consistent. In the LR 2 case, more output voltage magnitudes are covered because of the broader FOV. The maximum switching frequency happens around the $V_{dc}/3$ curve, which is about 10 kHz to 11 kHz for both LR 1 and LR 2 cases. And the switching frequency decreases in both directions that the output voltage magnitude increases or decreases away from $V_{dc}/3$. Some differences exist because of the disturbance on the grid voltage and the mismatch of the model parameters.

B. Impacts of Variable Switching Frequency Property

A significant impact of the variable switching frequency is analyzed on the switching loss, of which results are shown in Fig. 19. Fig. 19(a) displays the switching loss distribution of phase A semiconductor devices under the 1-*pf* trajectory with LR 1. It is noted that with the current magnitude increasing, the switching losses for all IGBTs and diodes are not proportionally increasing. The maximum switching loss happens when the current magnitude is around 11 A since the switching frequency decreases more and more according to the Fig. 16(a). Fig. 19(b) displays the switching loss

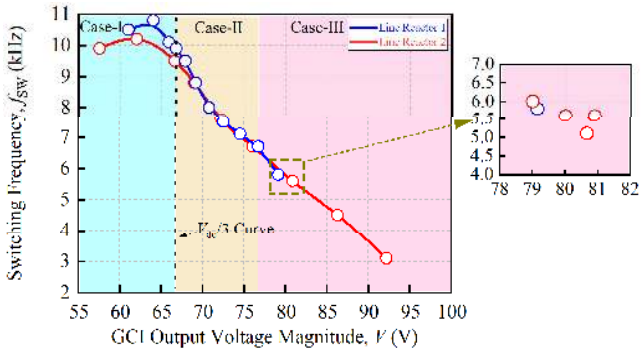

Fig. 18 Switching frequency over the output voltage magnitude.

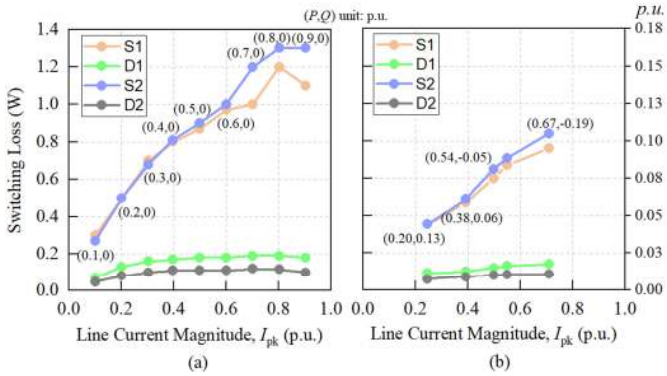

Fig. 19 Switching loss distribution of one-phase semiconductor devices (S1, D1, S2, and D2) under (a) 1-*pf* trajectory with LR 1 and (b) $0.4V_{dc}$ curve with LR 2 (base: rated single device loss 8 W).

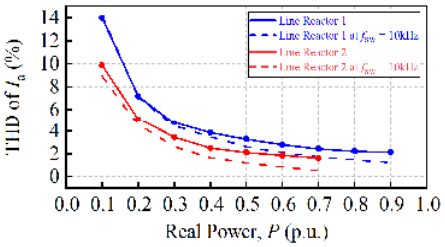

Fig. 20 THD of phase A current under 1-*pf* trajectory by FCS-MPC (solid) and fixed 10-kHz switching frequency modulation (dash).

distribution under the $0.4V_{dc}$ curve. It is noted that the switching loss has a quite linear relationship to the current magnitude, which results from about the same range of switching frequencies for these operating points in Fig. 17.

Another impact of this variable switching frequency is preliminarily investigated on the current harmonics. Fig. 20 reveals the THD of the phase A current under 1-*pf* in both LR 1 and LR 2 cases. Dash lines represent the THD of the phase A current by a fixed 10-kHz switching frequency modulation. THD values by FCS-MPC are higher than the one under the fixed 10-kHz modulation, especially for the high power loadings, This is because the switching frequency decreases by FCS-MPC with the power loading increasing. Then, the switching frequency component shifts to a lower order on the spectrum and take more weightings in the THD. A more sophisticated study on the harmonics for the FCS-MPC regulated converter will be conducted in the future work.

When the variable switching frequency property of FCS-MPC is not clear, it poses significant challenges on the filter design due to the uncertainty of the switching frequency. The filter has to consider the worst scenario with a broad variation range resulting in a very bulky and lossy filter design. With the contribution of this proposed variable switching frequency property, the maximal switching frequency $f_{sw,max}$ of the converter for the specific feasible operation region can be identified, which is when the magnitude of the converter output voltage is closest to the $V_{dc}/3$ curve. Then, the filter resonant frequency f_{res} generally should be sized lower than this maximal switching frequency but far above the grid fundamental frequency f_g to avoid the any resonance, such as $10f_g \le f_{res} \le 0.5f_{sw,max}$. In the meantime, the converter output complies with the grid code such as national standard IEEE 1547 and IEEE STD 519-1992, which also should be considered in the specification of the filter resonant frequency and harmonic attenuation ratio. In brief, the capability of identifying the maximum switching frequency of the grid converter by FCS-MPC control can significantly benefit the grid filter design.

C. Application of Variable Switching Frequency Property

Applying this variable switching frequency property of FCS-MPC to the industry application, its advantage would be prominent from the perspective of the thermal stress of power modules on the grid-connected inverter. During the high power loadings, FCS-MPC would autonomously decrease the switching frequency and further the power loss. During the low power loadings, FCS-MPC would increase the switching frequency and further the power loss. A more balanced thermal profile is achieved according to the proposed variable switching frequency property, which contributes to a reduced thermal stress on the power module in the long-term operation and eventually an enhanced reliability of the power converter without any additional active thermal controls.

Figs. 21-23 demonstrate this advantage by loading a varying mission profile, Fig. 21(a), on the inverter with LR 1 from Fig. 14. FCS-MPC and PI linear controllers are calibrated separately to regulate the power flow from the DC-bus to the grid. PI linear controller uses the fixed switching frequency at 8 kHz which is equal to the mean value of the variable switching frequency results in Fig. 16(a) since in the long-term operation, the switching frequency over the time by FCS-MPC would be close to the mean value of the switching frequency over the power loading.

Fig. 21, 22, and 23 show the comparisons between FCS-MPC and PI controllers on the averaged single IGBT loss, the thermal profiles, and the tradeoff analysis. Fig. 21(a) illustrates that both controllers achieve the stable power transmission according to the mission profile. The single IGBT loss in Fig. 21(b) reflects the distinction by FCS-MPC, that the switching frequency is higher than 8 kHz in the low power loading, and conversely lower than 8 kHz in the high power loading due to its variable switching frequency property. This result directly contributes to a lower thermal stress of power modules by FCS-MPC as shown in Fig. 22.

This article has been accepted for publication in a future issue of this journal, but has not been fully edited. Content may change prior to final publication. Citation information: DOI 10.1109/OJIA.2021.3091154, IEEE Open Journal of Industry Applications

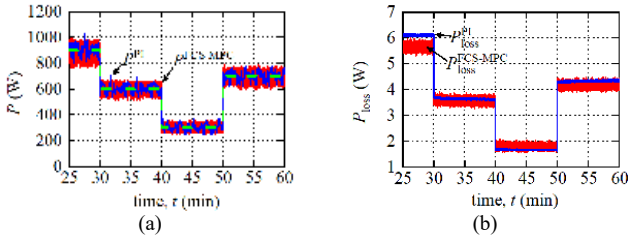

Fig. 21 Experimental results of the application over the mission profile, (a) the instantaneous real power by PI (blue) and FCS-MPC (red), (b) the averaged single IGBT loss by PI (blue) and FCS-MPC (red).

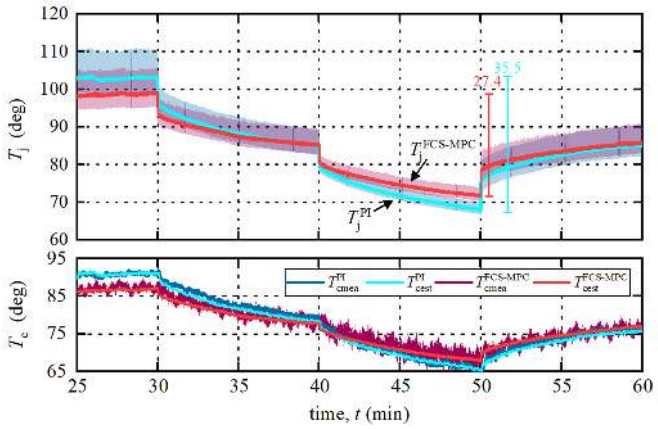

Fig. 22 Thermal profiles over the mission profile, the estimated junction temperatures, the estimated case temperatures and the measured case temperatures by PI and FCS-MPC, respectively.

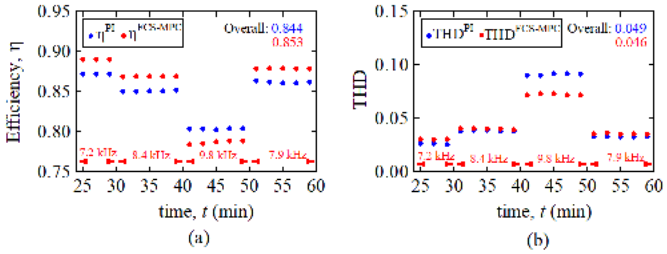

Fig. 23 Analysis over the varying mission profile by PI (blue) and FCS-MPC (red), (a) system efficiencies and (b) total harmonics distortions.

The junction temperature T_j in Fig. 22 is estimated through the RC thermal model and the heatsink temperature feedback. It is noted that the junction temperature variation is reduced to 27.4°C by FCS-MPC instead of 35.5°C by PI at around the same mean value. The high consistence of the estimated and measured case temperatures T_c strengthens the accuracy and the authenticity of the conclusions from the junction temperature. The overall system efficiencies (84.4% for PI and 85.3% for FCS-MPC) and THD (4.9% for PI and 4.6% for FCS-MPC) are noticed in Fig. 23 over the whole mission profile, where the system efficiency and the THD are not sacrificed by variable switching frequency property of FCS-MPC.

Thus, for those applications such as machine side converters and motor drives, broader and dynamic feasible operation regions are derived and FCS-MPC could achieve a superior performance on the thermal profile of power modules compared with the conventional PI controller. The thermal stress in the long-term operation, such as in the yearly time scale, could be reduced significantly, even for a limited feasible operation region.

VI. Conclusions

In this article, the variable switching frequency property of the finite control set model predictive control has been investigated. The intuitive relationship between the switching frequency and the magnitude of the converter output voltage reference is proposed through the geometry analysis, by the switching state selection and the switching sequence formulation. The switching frequency is derived to be maximized when the magnitude of the converter output voltage reference is around one-third of the DC-bus voltage value. Then, the switching frequency decreases in both directions that the magnitude moves away from this value. Multiple operating points from the contoured feasible operation range are tested in both simulations and experiments. All results verify the proposed variable switching frequency property of FCS-MPC.

The impacts of this property on the power loss and current harmonics are also analyzed, which provides engineers and researchers with more insights to fully leverage the FCS-MPC. One application of this proposed variable switching frequency property is presented to demonstrate the lower thermal stress of power modules by FCS-MPC compared with the conventional PI controller, where a less-varying temperature profile is achieved over the same mission profile. This contribution can benefit the reliability of power converters in the industry application for the long-term operation.

Appendix

FOV

The voltage limit curve in FOV is shown in (26) and can be rearranged as follows,

$$\frac{(V_d)^2}{(V_{dc}/\sqrt{3})^2}+\frac{(V_q)^2}{(V_{dc}/\sqrt{3})^2}\leqslant 1 \tag{32}$$

which is a circle with the center at the origin (0, 0) and the radius of $V_{dc}/\sqrt{3}$. Similarly, the $V_{dc}/3$ curve can be derived,

$$\frac{(V_d)^2}{(V_{dc}/3)^2}+\frac{(V_q)^2}{(V_{dc}/3)^2}\leqslant 1 \tag{33}$$

which is a circle with the center at the origin (0, 0) and the radius of $V_{dc}/3$. The current limit curve in FOV is shown in (27), where I_d and I_q can be calculated in perspectives of V_d and V_q in the steady state through the following equations,

$$\begin{aligned} V_d &= E_d + R_g I_d - w_s L_g I_q \\ V_q &= E_q + R_g I_q + w_s L_g I_d \end{aligned} \tag{34}$$

Then, I_d and I_q can be represented into the following,

$$I_d = \frac{R_g(V_d - E_d) + w_s L_g(V_q - E_q)}{R_g^2 + (w_s L_g)^2}$$
$$I_q = \frac{R_g(V_q - E_q) - w_s L_g(V_d - E_d)}{R_g^2 + (w_s L_g)^2} \quad (35)$$

In the most grid-connected applications, the line reactance is much greater than the line resistance, which is $w_s L_g >> R_g$. Equation (35) can be further simplified as follows,

$$I_d = \frac{(V_q - E_q)}{(w_s L_g)}, \quad I_q = \frac{-(V_d - E_d)}{(w_s L_g)} \quad (36)$$

Equation (28) can be derived eventually by applying (36) to (27), which is a circle with the center at (E_d, E_q) and the radius of $w_s L_g I_{max}$.

REFERENCES

[1] F. Blaabjerg, R. Teodorescu, M. Liserre and A. V. Timbus, "Overview of Control and Grid Synchronization for Distributed Power Generation Systems," *IEEE Trans. Ind. Electron.*, vol. 53, no. 5, pp. 1398-1409, Oct. 2006.

[2] A. Timbus, M. Liserre, R. Teodorescu, P. Rodriguez and F. Blaabjerg, "Evaluation of Current Controllers for Distributed Power Generation Systems," *IEEE Trans. Power Electron.*, vol. 24, no. 3, pp. 654-664, March 2009.

[3] M. G. Simoes, B. K. Bose and R. J. Spiegel, "Fuzzy logic based intelligent control of a variable speed cage machine wind generation system," *IEEE Trans. Power Electron.*, vol. 12, no. 1, pp. 87-95, Jan. 1997.

[4] J. R. Massing, M. Stefanello, H. A. Grundling and H. Pinheiro, "Adaptive Current Control for Grid-Connected Converters With LCL Filter," *IEEE Trans. Ind. Electron.*, vol. 59, no. 12, pp. 4681-4693, Dec. 2012.

[5] J. Hu, L. Shang, Y. He and Z. Q. Zhu, "Direct Active and Reactive Power Regulation of Grid-Connected DC/AC Converters Using Sliding Mode Control Approach," *IEEE Trans. Power Electron.*, vol. 26, no. 1, pp. 210-222, Jan. 2011.

[6] X. Fu and S. Li, "Control of Single-Phase Grid-Connected Converters With LCL Filters Using Recurrent Neural Network and Conventional Control Methods," *IEEE Trans. Power Electron.*, vol. 31, no. 7, pp. 5354-5364, July 2016.

[7] J. Rodriguez, J. Pontt, C. A. Silva, P. Correa, P. Lezana, P. Cortes, and U. Ammann, "Predictive Current Control of a Voltage Source Inverter," *IEEE Trans. Ind. Electron.*, vol. 54, no. 1, pp. 495-503, Feb. 2007.

[8] P. Cortes, M. P. Kazmierkowski, R. M. Kennel, D. E. Quevedo and J. Rodriguez, "Predictive Control in Power Electronics and Drives," *IEEE Trans. Ind. Electron.*, vol. 55, no. 12, pp. 4312-4324, Dec. 2008.

[9] S. Kouro, P. Cortes, R. Vargas, U. Ammann and J. Rodriguez, "Model Predictive Control—A Simple and Powerful Method to Control Power Converters," *IEEE Trans. Ind. Electron.*, vol. 56, no. 6, pp. 1826-1838, June 2009.

[10] J. Rodriguez, M. P. Kazmierkowski, J. R. Espinoza, P. Zanchetta, H. Abu-Rub, H. A. Young, and C. A. Rojas, "State of the Art of Finite Control Set Model Predictive Control in Power Electronics," *IEEE Trans. Ind. Inf.*, vol. 9, no. 2, pp. 1003-1016, May 2013.

[11] S. Vazquez, J. I. Leon, L. G. Franquelo, J. Rodriguez, H. A. Young, A. Marquez, and P. Zanchetta, "Model Predictive Control: A Review of Its Applications in Power Electronics," *IEEE Ind. Electron Magazine*, vol. 8, no. 1, pp. 16-31, March 2014.

[12] S. Kouro, M. A. Perez, J. Rodriguez, A. M. Llor and H. A. Young, "Model Predictive Control: MPC's Role in the Evolution of Power Electronics," *IEEE Ind. Electron. Mag.*, vol. 9, no. 4, pp. 8-21, Dec. 2015

[13] S. Vazquez, J. Rodriguez, M. Rivera, L. G. Franquelo and M. Norambuena, "Model Predictive Control for Power Converters and Drives: Advances and Trends," *IEEE Trans. Ind. Electron.*, vol. 64, no. 2, pp. 935-947, Feb. 2017.

[14] P. Karamanakos, E. Liegmann, T. Geyer and R. Kennel, "Model Predictive Control of Power Electronic Systems: Methods, Results, and Challenges," *IEEE Open Journal of Industry Applications*, vol. 1, pp. 95-114, 2020.

[15] T. Geyer and D. E. Quevedo, "Multistep Finite Control Set Model Predictive Control for Power Electronics," *IEEE Trans. Power Electron.*, vol. 29, no. 12, pp. 6836-6846, Dec. 2014.

[16] M. Narimani, B. Wu, V. Yaramasu, Z. Cheng, and N. R. Zargari, "Finite control-set model predictive control (FCS-MPC) of nested neutral point-clamped (NNPC) converter," *IEEE Trans. Power Electron.*, vol. 30, no. 12, pp. 7262–7269, Dec. 2015.

[17] B. Stellato, T. Geyer, and P. J. Goulart, "High-speed finite control set model predictive control for power electronics," *IEEE Trans. Power Electron.*, vol. 32, no. 5, pp. 4007–4020, May 2017.

[18] M. Siami, D. A. Khaburi, and J. Rodríguez, "Simplified finite control set-model predictive control for matrix converter-fed PMSM drives," *IEEE Trans. Power Electron.*, vol. 33, no. 3, pp. 2438–2446, Mar. 2018.

[19] A. A. Ahmed, B. K. Koh and Y. I. Lee, "A Comparison of Finite Control Set and Continuous Control Set Model Predictive Control Schemes for Speed Control of Induction Motors," *IEEE Trans. Ind. Inf.*, vol. 14, no. 4, pp. 1334-1346, April 2018.

[20] P. Karamanakos and T. Geyer, "Guidelines for the design of finite control set model predictive controllers," *IEEE Trans. Power Electron.*, vol. 35, no. 7, pp. 7434–7450, Jul. 2020.

[21] D.-K. Choi and K.-B. Lee, "Dynamic performance improvement of ac/dc converter using model predictive direct power control with finite control set," *IEEE Trans. Ind. Electron.*, vol. 62, no. 2, pp. 757–767, Feb. 2015.

[22] P. Falkowski and A. Sikorski, "Finite control set model predictive control for grid-connected ac-dc converters with *LCL* filter," *IEEE Trans. Ind. Electron.*, vol. 65, no. 4, pp. 2844–2852, Apr. 2018.

[23] T. Dragičević, "Model Predictive Control of Power Converters for Robust and Fast Operation of AC Microgrids," *IEEE Trans. Power Electron.*, vol. 33, no. 7, pp. 6304-6317, July 2018.

[24] P. Cortés, G. Ortiz, J. I. Yuz, J. Rodríguez, S. Vazquez, and L. G. Franquelo, "Model predictive control of an inverter with output *LC* filter for UPS applications," *IEEE Trans. Ind. Electron.*, vol. 56, no. 6, pp. 1875–1883, Jun. 2009.

[25] C. Zheng, T. Dragičević, and F. Blaabjerg, "Current-sensorless finite set model predictive control for *LC*-filtered voltage source inverters," *IEEE Trans. Power Electron.*, vol. 35, no. 1, pp. 1086–1095, Jan. 2020.

[26] J. Qin and M. Saeedifard, "Predictive control of a modular multilevel converter for a back-to-back HVDC system," *IEEE Trans. Power Del.*, vol. 27, no. 3, pp. 1538–1647, Jul. 2012.

[27] Y. Zhang, X.Wu, X. Yuan, Y.Wang, and P. Dai, "Fast model predictive control for multilevel cascaded H-bridge STATCOM with polynomial computation time," *IEEE Trans. Ind. Electron.*, vol. 63, no. 8, pp. 5231–5243, Aug. 2016.

[28] J. Falck, G. Buticchi and M. Liserre, "Thermal Stress Based Model Predictive Control of Electric Drives," *IEEE Trans. Ind. Appl.*, vol. 54, no. 2, pp. 1513-1522, March-April 2018.

[29] L. Wang, J. He, T. Han and T. Zhao, "Finite Control Set Model Predictive Control With Secondary Problem Formulation for Power Loss and Thermal Stress Reductions," *IEEE Trans. Ind. Appl.*, vol. 56, no. 4, pp. 4028-4039, July-Aug. 2020.

[30] M. Preindl and S. Bolognani, "Model Predictive Direct Speed Control with Finite Control Set of PMSM Drive Systems," *IEEE Tran. Power Electron.*, vol. 28, no. 2, pp. 1007-1015, Feb. 2013

[31] M. Preindl and S. Bolognani, "Model Predictive Direct Torque Control With Finite Control Set for PMSM Drive Systems, Part 1: Maximum Torque Per Ampere Operation," *IEEE Trans. Ind. Inf.*, vol. 9, no. 4, pp. 1912-1921, Nov. 2013.

[32] M. Preindl and S. Bolognani, "Model Predictive Direct Torque Control With Finite Control Set for PMSM Drive Systems, Part 2: Field Weakening Operation," *IEEE Trans. Ind. Inf.*, vol. 9, no. 2, pp. 648-657, May 2013.

[33] A. Andersson and T. Thiringer, "Assessment of an improved finite control set model predictive current controller for automotive

propulsion applications," *IEEE Trans. Ind. Electron.*, vol. 67, no. 1, pp. 91–100, Jan. 2020.

[34] Z. Song, C. Xia and T. Liu, "Predictive Current Control of Three-Phase Grid-Connected Converters With Constant Switching Frequency for Wind Energy Systems," *IEEE Trans. Ind. Electron.*, vol. 60, no. 6, pp. 2451-2464, June 2013.

[35] Z. Ma, S. Saeidi and R. Kennel, "FPGA Implementation of Model Predictive Control With Constant Switching Frequency for PMSM Drives," *IEEE Trans. Ind. Inf.*, vol. 10, no. 4, pp. 2055-2063, Nov. 2014.

[36] M. Tomlinson, H. d. T. Mouton, R. Kennel and P. Stolze, "A Fixed Switching Frequency Scheme for Finite-Control-Set Model Predictive Control—Concept and Algorithm," *IEEE Trans. Ind. Electron*, vol. 63, no. 12, pp. 7662-7670, Dec. 2016.

[37] L. Tarisciotti, A. Formentini, A. Gaeta, M. Degano, P. Zanchetta, R. Rabbeni, M. Pucci, "Model Predictive Control for Shunt Active Filters With Fixed Switching Frequency," *IEEE Trans. Ind. Appl.*, vol. 53, no. 1, pp. 296-304, Jan.-Feb. 2017.

[38] Donoso, A. Mora, R. Cárdenas, A. Angulo, D. Sáez and M. Rivera, "Finite-Set Model-Predictive Control Strategies for a 3L-NPC Inverter Operating With Fixed Switching Frequency," *IEEE Tran. Ind. Electron.*, vol. 65, no. 5, pp. 3954-3965, May 2018.

[39] P. Karamanakos, R. Mattila, and T. Geyer, "Fixed switching frequency direct model predictive control based on output current gradients," *Proc. IEEE Ind. Electron. Conf.*, Washington, D.C., USA, Oct. 2018, pp. 2329–2334.

[40] M. Aguirre, S. Kouro, C. A. Rojas, J. Rodriguez and J. I. Leon, "Switching Frequency Regulation for FCS-MPC Based on a Period Control Approach," in *IEEE Tran. Ind. Electron*, vol. 65, no. 7, pp. 5764-5773, July 2018.

[41] M. Aguirre, S. Kouro, C. A. Rojas and S. Vazquez, "Enhanced Switching Frequency Control in FCS-MPC for Power Converters," *IEEE Trans. Ind. Electron,* vol. 68, no. 3, pp. 2470-2479, March 2021.

[42] A. Calle-Prado, S. Alepuz, J. Bordonau, J. Nicolas-Apruzzese, P. Cortés and J. Rodriguez, "Model Predictive Current Control of Grid-Connected Neutral-Point-Clamped Converters to Meet Low-Voltage Ride-Through Requirements," *IEEE Trans. Ind. Electron.*, vol. 62, no. 3, pp. 1503-1514, March 2015.

[43] S. C. Ferreira, R. B. Gonzatti, R. R. Pereira, C. H. da Silva, L. E. B. da Silva and G. Lambert-Torres, "Finite Control Set Model Predictive Control for Dynamic Reactive Power Compensation With Hybrid Active Power Filters," *IEEE Trans. Ind. Electron.*, vol. 65, no. 3, pp. 2608-2617, March 2018.

[44] M. Metry, M. B. Shadmand, R. S. Balog and H. Abu-Rub, "MPPT of Photovoltaic Systems Using Sensorless Current-Based Model Predictive Control," *IEEE Trans. Ind. Appl.*, vol. 53, no. 2, pp. 1157-1167, March-April 2017.

[45] Southeast National Marine Renewable Energy Center, "Resource measurement & modeling: Available data," ADCP-0001B2&B3 (November 2011-April 2012). Nov. 2013. [Online]. Available: http://coet.fau.edu/resource-measurement-modeling/available-data.html.

[46] ABB HiPak 5SND0800M170100 IGBT Module. [Online]. Available: https://new.abb.com/products/5SND0800M170100/dual-hipak-igbt-module.

[47] Infineon IKCM15L60GD Intelligent Power Module. [Online]. Available: https://www.infineon.com/cms/en/product/power/intelligent-power-modules-ipm/ikcm15l60gd/.

[48] A. Sayed-Ahmed, L. Wei and B. Seibel, "Industrial regenerative motor-drive systems," *2012 Twenty-Seventh Annual IEEE Applied Power Electronics Conference and Exposition (APEC)*, 2012, pp. 1555-1561.

[49] K. Ma, M. Liserre, F. Blaabjerg and T. Kerekes, "Thermal Loading and Lifetime Estimation for Power Device Considering Mission Profiles in Wind Power Converter," *IEEE Trans. Power Electron.*, vol. 30, no. 2, pp. 590-602, Feb. 2015.

Luocheng Wang (S'17) received the B.S. degree in electrical engineering from University of Connecticut, Storrs, CT, USA, in 2014 and the M.Eng. degree in electrical and computer engineering from Cornell University, Ithaca, NY, USA, in 2016. He is currently pursuing the Ph.D. degree in electrical and computer engineering at the University of North Carolina at Charlotte, Charlotte, NC, USA.

His current research interests include advanced control of power converters and electrical drives, model predictive control, reliability in power electronics, grid-integration of renewable energy systems and inductive power transfer.

Tiefu Zhao (S'06–M'10–SM'12) received the B.S. and M.S. degrees from Tsinghua University, Beijing, China, in 2003 and 2005, respectively, and the Ph.D. degree from North Carolina State University, Raleigh, in 2010, all in electrical engineering.

From 2010 to 2016, he was with Eaton Corporation Research & Technology, Milwaukee, WI. Since 2016, he has been an Assistant Professor of Electrical and Computer Engineering and an Associate of the Energy Production and Infrastructure Center (EPIC) with the University of North Carolina at Charlotte, Charlotte, NC, USA. He has published over 40 papers in refereed journals and international conference proceedings. He has 12 patents awarded. His current research interests include solid state transformer and solid state circuit protection, wireless power transfer, microgrid and renewable energy integration, wide bandgap device applications and power electronics reliability.

Dr. Zhao was the recipient of 2015 IAS Andrew W. Smith Outstanding Young Member Award and 2015 STEM Forward Young Engineer of the Year Award. Dr. Zhao has served as an Associate Editor for the IEEE Journal of Emerging and Selected Topics in Power Electronics (JESTPE). He has served as the Organizing Committee Member on several international conferences, including ECCE 2016-2019 and PEDG 2018. He is the Founding Chair of IEEE Charlotte section PELS/IAS/IES Chapter.

Jiangbiao He (S'08–M'15–SM'16) received the Ph.D. degree in electrical engineering with an emphasis on power energy conversion from Marquette University, Milwaukee, WI, USA. He is currently an Assistant Professor with the Department of Electrical and Computer Engineering at the University of Kentucky, USA. He previously worked in industry, most recently as a Lead Engineer at GE Global Research, Niskayuna, New York. He also worked at Rockwell Automation and Eaton Corporate Research before he joined GE in 2015.

His research interests include transportation electrification, renewable energy, and fault-tolerant operation of power conversion systems for safety-critical applications.